



Lattice Boltzmann study of mass transfer for two-dimensional Bretherton/Taylor bubble train flow

A. Kuzmin^{a,*}, M. Januszewski^b, D. Eskin^c, F. Mostowfi^c, J.J. Derksen^a

^aChemical and Materials Engineering, University of Alberta, 7th Floor, ECERF, 9107 116 St, Edmonton, Alberta, Canada T6G 2V4

^bInstitute of Physics, University of Silesia, 40-007 Katowice, Poland

^cSchlumberger DBR Technology Center, 9450 17 Ave NW, Edmonton, Alberta, Canada T6N 1M9

HIGHLIGHTS

- We simulate gas–liquid mass transfer for bubble train flow.
- The bubble shapes are obtained numerically without analytical simplifications.
- The lattice Boltzmann method was used for mass transfer and flow simulations.
- One unit cell simulations are enough to obtain the correct mass transfer coefficient.

ARTICLE INFO

Article history:

Received 3 August 2012

Received in revised form 25 March 2013

Accepted 30 March 2013

Available online 11 April 2013

Keywords:

Mass Transfer

Taylor/Bretherton bubble train flow

Multiphase flow

Lattice Boltzmann method

Binary liquid model

Flow in microchannels with parallel plates

ABSTRACT

This work presents a procedure for the determination of the volumetric mass transfer coefficient in the context of lattice Boltzmann simulations for the Bretherton/Taylor bubble train flow for capillary numbers $0.1 < Ca < 1.0$. We address the case where the hydrodynamic pattern changes from having a vortex in the slug ($Ca < 0.7$) to not having it ($Ca > 0.7$) [1]. In the latter case the bubble shape is asymmetric and cannot be approximated through flat surfaces and circular circumferences as is often done in the literature [2,3]. When the vortex is present in the slug, the scalar concentration is well mixed and it is common to use periodic boundary conditions and the inlet/outlet-averaged concentration as the characteristic concentration. The latter is not valid for flows where the tracer is not well mixed, i.e. $Ca > 0.7$. We therefore examine various boundary conditions (periodic, open, open with more than 1 unit cell) and definitions of the characteristic concentration to estimate mass transfer coefficients for the range of capillary numbers $0.1 < Ca < 1.0$. We show that the time-dependent volume averaged concentration taken as the characteristic concentration produces the most robust results and that all strategies presented in the literature are extreme limits of one unified equation. Finally, we show good agreement of simulation results for different Peclet numbers with analytical predictions of van Baten and Krishna [2].

© 2013 Elsevier B.V. All rights reserved.

1. Introduction

Monolith reactors have recently been getting more attention as a promising alternative to slurry reactors and trickle bed reactors [3,4]. These reactors usually operate in the Bretherton–Taylor regime [5,6] which is a flow of equally sized, long air bubbles through a liquid medium, see Fig. 1. This flow regime is characterized by the dominance of surface tension over inertia and viscous effects, and by comparatively small gas flow velocities [7]. Due to the dominance of surface tension, the flow exhibits advantageous properties which cannot be achieved in its macroscopic counterparts: thin

liquid films [5] between bubbles and walls strongly enhance mass transfer from gas and walls to liquid; the plug flow regime occurring in monolith reactors allows to perform chemical reactions in slugs only [3]. Moreover, the low slip velocity between gas and liquid is utilized in experiments to measure liquid velocity [6]: bubbles traveling with approximately the same velocity as liquid can be captured with a camera. These properties explain why nowadays one can find a large number of applications of the Bretherton–Taylor bubble train flow: continuous flow analyzers to measure liquid velocity, chemical reactors for hydrogenation of nitroaromatics, 2-ethyl-hexenal, Fischer–Tropsch synthesis, etc. The extensive reviews of Kreutzer et al. [3], Gupta et al. [8], Yue et al. [7] cover a significant number of applications.

This work is focused on gas to liquid mass transfer for the two-dimensional Bretherton/Taylor flow. A good understanding of mass transfer and how it depends on parameters such as the capillary

* Corresponding author. Tel.: +1 438 824 3695.

E-mail addresses: kuzmin@ualberta.ca (A. Kuzmin), michalj@gmail.com (M. Januszewski), deskin@slb.com (D. Eskin), fmstowfi@slb.com (F. Mostowfi), jos@ualberta.ca (J.J. Derksen).

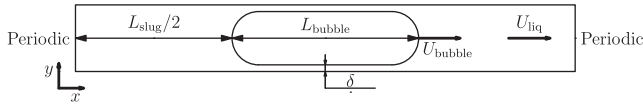


Fig. 1. Simplified sketch of the bubble motion. Using periodic conditions for the velocity field is natural, but needs evaluation for mass transfer.

number, the Reynolds number, and slug and bubble lengths allows to properly manufacture a microchannel with properties necessary to ensure that chemical reactions are performed in the best possible manner. The mass transfer coefficient is defined as the flux from the gas–liquid interface divided by the difference of the imposed concentration and the characteristic concentration in the domain. The concentration distribution in the domain is prescribed by underlying hydrodynamics fields. For example, experimental studies [7,4] show a complex dependency of the mass transfer coefficient on flow parameters: bubble and slug lengths, and bubble velocity, which in turn relate to the capillary number Ca and the Reynolds number Re . Yue et al. [7] established an experimental correlation for the volumetric mass transfer coefficient for a bubble train as a function of the diffusion coefficient, slug and bubble lengths, and bubble velocity:

$$k_L a = \frac{2}{d_h} \left(\frac{DU_{\text{bubble}}}{L_{\text{bubble}} + L_{\text{slug}}} \right)^{0.5} \left(\frac{L_{\text{bubble}}}{L_{\text{bubble}} + L_{\text{slug}}} \right)^{0.3}, \quad (1)$$

where $k_L a$ is the volumetric mass transfer coefficient, d_h is the hydraulic diameter, L_{bubble} is the bubble length, L_{slug} is the slug distance (between bubbles), U_{bubble} is the bubble velocity, and D is the diffusion coefficient.

The understanding of mass transfer for the bubble train flow is not possible without knowledge of hydrodynamic patterns. There are several works studying the hydrodynamic properties of the bubble train flow, both experimental [9–11] and numerical [12,13,14,15]. For the flow of long bubbles between parallel plates chosen here as the study case, it is indicated that there exists a vortex in the liquid slug for $Ca < 0.7$, and that the bubble shape is symmetric for low capillary numbers ($Ca < 0.1$ [11]) with the capillary number defined as:

$$Ca = \frac{\mu_{\text{liq}} U_{\text{bubble}}}{\gamma}, \quad (2)$$

where μ_{liq} is the liquid viscosity, U_{bubble} is the bubble velocity, and γ is the interfacial tension. The fact that the bubble shape for $Ca < 0.1$ can be represented as two hemicircles and two planar interfaces with the vortex existing in the liquid slug has been utilized for analytical estimations of mass transfer properties.

Since the mass transfer coefficient is defined in terms of a mass flux through a certain area, see Section 2, analytical estimates [3,16] are based on a decomposition of the bubble surface in parts. The mass transfer coefficient is calculated through two separate contributions from two planar films and two hemicircles. For both contributions the Higbie penetration theory [17] is utilized, which states that the mass transfer coefficient for a simple flow geometry depends on the average time a liquid packet interacts with a geometrical feature. It can be calculated as $\sqrt{\frac{\pi D}{t_{\text{char}}}}$, where t_{char} is the interaction time. As an example of the application of the Higbie penetration theory, the mass transfer coefficient for the flow of bubbles between parallel plates is calculated as (similar to the work of van Baten and Krishna [2]):

$$k_L = 2\sqrt{\frac{\pi D}{t_{\text{film}}}} + 2\sqrt{\frac{\pi D}{t_{\text{circle}}}}, \quad (3)$$

where $t_{\text{film}} = \frac{L_{\text{film}}}{U_{\text{bubble}}}$ stands for the interaction time of liquid traveling next to the planar part of the bubble, and $t_{\text{circle}} = \frac{\pi R_{\text{circle}}}{U_{\text{bubble}}}$ is the time

during which the liquid in the slug travels the distance of half the bubble cap circumference.

Despite their simplicity, such analytical expressions work well for flows with low capillary numbers $Ca < 0.1$ [4] where the bubble shape is symmetrical and can be approximated with good precision. Moreover, because of the hydrodynamic pattern in the slug (i.e. presence of a vortex in the slug), one can estimate the time for a fluid batch to travel the whole circumference. However, with the increase of the capillary number the situation changes significantly – the symmetrical bubble shape is lost and the bubble resembles a bullet [18]. For flows with $Ca > 0.7$ there is also no vortex in the liquid slug. In this case the Higbie theory fails to estimate the contribution from bubble caps, which explains the need to turn to numerical simulations where all hydrodynamic fields as well as complex bubble shapes are taken into account.

Typical numerical studies of mass transfer [3,2] do not consider the simulation of bubble shapes for $Ca > 0.1$. The interesting work by Onea et al. [19] only takes into account short length bubbles in microchannels with a square cross-section. As well, in this work a Schmidt number of around 0.8 is used: thus, the thickness of the concentration and momentum boundary layer is similar leading to qualitative results since it's not possible to separate mixing due to hydrodynamics patterns from mixing due to diffusion.

The usual simulation of mass transfer is performed as follows:

- I The bubble shape is calculated either through analytical correlations [5] or experimental correlations [11] without directly resolving bubble shapes through multiphase simulations. The expressions for bubble shapes are available only for flows with capillary number $Ca < 0.1$.
- II Hydrodynamic fields are then obtained by performing simulations of one-component flow around the bubble by imposing the bubble velocity on the channel walls. Thus, the simulations are performed in the reference frame moving with the bubble. A stress-free condition is imposed at the bubble surface.
- III The mass transfer simulations are performed in the reference frame moving with the bubble. The saturation concentration is imposed at the bubble surface. Only one unit cell containing a single bubble is used for simulations. Periodic concentration boundary conditions are utilized to determine the volumetric mass transfer coefficient, which is calculated through the following equation [2]:

$$k_L a = \frac{\overline{\text{Flux}}}{C_{\text{bubble}} - \langle C_{\text{in/outlet}} \rangle} \frac{\text{bubble surface area}}{\text{unit cell volume}}, \quad (4)$$

where $\langle C_{\text{in/outlet}}(t) \rangle = \int C U_{\text{in/outlet}} dA / \int U_{\text{in/outlet}} dA$ is the space-averaged inlet/outlet (periodic boundary conditions) concentration as a function of time. Therefore, in terms of the mass transfer definition, $\langle C_{\text{in/outlet}}(t) \rangle$ plays the role of the characteristic concentration. The time-averaged concentration flux ($\overline{\text{Flux}}$) is calculated as the difference between the overall average concentration in the whole domain ($\langle C_{\text{overall}} \rangle = \int_V C dV / V$) at time t_1 and at time t_2 divided by the time difference $t_2 - t_1$. The agreement between numerical simulations [2] and experimental correlations of [4] was good.

The presented numerical approaches [2,3] can be criticized on a number of points. They mainly relate to the bubble shape approximation, which is taken to be symmetrical, i.e. consisting of two hemispheres and film for the case of flow in circular capillaries. This is valid for small capillary numbers only ($Ca < 0.1$). As previously discussed, for such capillary numbers the tracer is well mixed in the slug and the choice of the characteristic concentration needed for the mass transfer coefficient, Eq. (5), is obvious. With minimal differences in the results, it can either be the averaged

concentration in the liquid slug or the inlet/outlet space-averaged concentration. The latter is used in the formulation of van Baten and Krishna [2] presented above.

While it is clear that periodic boundary conditions can be employed for the calculation of hydrodynamic fields, the same does not apply to the mass transfer coefficient simulations. Experimental correlations [4] show that the concentration in a bubble train along the streamwise direction changes exponentially with distance. Mass transfer simulations however, are made only for one unit cell using periodic boundary conditions with the same concentration at the inlet and at the outlet. The question how a single unit cell simulation corresponds to experimental measurements arises where the concentration difference is measured at distances of at least a few unit cells [4]. In other words, one needs to understand how the discrete one unit cell simulation corresponds to the continuous picture in experiments where one does not distinguish discrete bubbles but takes measurements of concentration at different locations.

Addressing situations for a rich number of hydrodynamic patterns, shapes, and effects of bubble lengths, etc for bubble train flows, we feel that there is a need to examine carefully the strategies and assumptions behind the numerical calculations of the mass transfer coefficient. We aim at establishing clear procedures as to how properly obtain the mass transfer coefficient via a study of different boundary conditions and different definitions of the characteristic concentration. The case we want to examine is a two-dimensional bubble train flow between parallel plates. We address the following:

- I Applicability of periodic boundary conditions to determine the mass transfer coefficient when the vortex in the slug disappears, i.e. when $Ca > 0.7$.
- II Validity of the inlet/outlet-averaged or domain-averaged concentrations as characteristic concentrations in the definition of the mass transfer coefficient.
- III Translation of the continuous experimental picture to numerical simulations of a few unit cells, the issue of correspondence between space averages (simulations [2]) and time averages (experiment).

In addition, at the end of the manuscript we present results of the dependence of the volumetric mass transfer coefficient on the Peclet number that we compare with analytical [16] and experimental correlations [7]. The thorough determination of the mass transfer coefficient and associated Sherwood number as a function of other non-dimensional parameters such as gas holdup, bubble/slug lengths, and the capillary number is left for future studies.

To establish numerical procedures we performed multiphase simulations to extract bubble shapes [18,13] for the range of capillary numbers $Ca = 0.1–1.0$. For this range of capillary numbers we were able to capture the bubble shape change and the change of hydrodynamic patterns. The mass transfer simulations presented here were performed with various boundary conditions (open, periodic) and with a few unit cells (1–10 unit cells). As our numerical approach we take the lattice Boltzmann method, a relatively new CFD competitor developed during the last 20 years [20–23]. This method was successfully applied to simulate not only single phase hydrodynamic problems [24], but also multiphase flows [25–27], heat transfer [28,29], and ferrofluids [30,31].

Mass transfer problems in the lattice Boltzmann framework were mainly addressed in a series of works of Ginzburg and co-authors [32–34]. In contrast to these works whose focus was on simulating the advection-diffusion equation via the lattice Boltzmann framework, we concentrate on the application side. One should also mention the work of [35] about heat and mass transfers in porous media and the work of [36] simulating lateral mixing

in cross-channel flow. The last two works are focused on problems of homogeneous nature and do not provide guidance as to how to obtain the mass transfer coefficient for heterogeneous cases.

The paper is organized as follows. We start with definitions of the volumetric mass transfer coefficient and apply them to bubble train flow in order to derive expressions to connect space- and time-averages. Then, the lattice Boltzmann model used to simulate mass transfer is presented, followed by benchmarks. Finally, numerical simulations of various boundary conditions and simulations spanning a few unit cells for different hydrodynamic patterns are presented to establish the procedure to determine the volumetric mass transfer coefficient. The comparison with analytical correlations is also discussed.

2. Mass transfer definitions

By definition, the mass transfer coefficient from a surface with an imposed constant concentration C_{bubble} is:

$$k_L = \frac{\dot{m}}{P\Delta C}, \quad \Delta C = C_{\text{bubble}} - C_{\text{medium}}, \quad (5)$$

where \dot{m} is the mass flux [kg s^{-1}], P is the area of the surface [m^2], and ΔC is the concentration difference between the surface and the surrounding medium [kg m^{-3}]. Therefore, k_L has units of [m s^{-1}]. Usually, the surrounding medium concentration is taken at an infinite distance from the bubble. However, in the case of complicated geometries and non-homogeneous concentrations, the medium concentration can be the average concentration in the domain or the flux-averaged concentration at the inlet or outlet, etc. Thus, one needs to establish a clear definition of ΔC to determine the volumetric mass transfer coefficient in the case of complex geometries and non-trivial hydrodynamic velocity patterns.

We first examine the definitions of mass transfer in the case of point sources.

2.1. Point mass sources

In what follows we will present three approaches to calculate point mass transfer coefficients (by point source we assume the source to have an infinitesimally small surface area P):

1. Let us look at the infinitesimally small domain of volume $A \Delta x$, not moving and containing a point source. The concentration difference is $\Delta C = C^* - C(t)$, where C^* is the imposed point source concentration, and $C(t)$ is the time-dependent concentration, which does not depend on the location due to the assumption of homogeneity. One can therefore write a time-dependent ordinary differential equation for the concentration in the domain:

$$\dot{m} = A\Delta x \frac{dC}{dt} = k_L P (C^* - C(t)), \quad (6)$$

with the initial condition $C(0) = 0$. The solution can be found as:

$$C(t) = C^* (1 - \exp(-k_L a t)), \quad (7)$$

where $k_L a$ is the volumetric mass transfer coefficient defined as:

$$k_L a = k_L \frac{P}{A\Delta x} = k_L \frac{P}{V}, \quad (8)$$

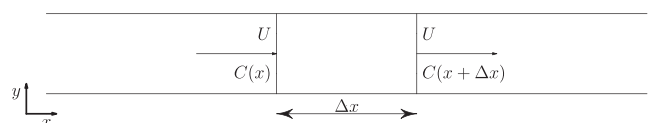


Fig. 2. The mass transfer in a moving liquid.

where P is the source surface, V is the unit cell volume.

2. Let us predict mass transfer in a liquid moving with the velocity U , see Fig. 2.

If one can assume that the point mass sources are homogeneously distributed in the whole medium, the mass accumulated in the volume $V=A\Delta x$ can be calculated as the difference of mass fluxes entering and leaving the domain $U(C(x+\Delta x) - C(x))$. The accumulated mass should be proportional to the mass transfer coefficient:

$$U(C(x+\Delta x) - C(x)) = k_L P(C^* - C(x)), \quad (9)$$

giving the same solution, now in the spatial domain:

$$C(x) = C^* \left(1 - \exp\left(-k_L a \frac{x}{U}\right) \right). \quad (10)$$

Note that the concentration $C(x)$ does not depend on time.

3. If one transfers to the frame moving with the liquid velocity U , the situation will be the same as in the first case. One can connect time and space with the velocity U ($t = \frac{x}{U}$).

2.2. Bubble train

In the application to bubble train flow it is useful to think of one bubble as a point source to be able to use the calculations presented above. For example, the expression (10) was used in experiments by [4]. However, one should be accurate with the definition of velocities because two different phases co-exist in the bubble train flow. Usually, one can take the velocity U to be a bulk velocity or $U = U_{\text{gas}} + U_{\text{liq}}$, where U_{gas} and U_{liq} are liquid and gas superficial velocities, respectively. The gas and liquid superficial and actual velocities are connected with each other through a complex dependency on Ca , ϵ [13].

With experimental measurements of concentration at different locations, the calculation of the mass transfer coefficient using the logarithmic function is straightforward. However, if one wants to analytically or numerically calculate the mass transfer coefficients, the situation is much more complicated because of the presence of two phases and complex bubble geometry. As was mentioned before, depending on the capillary number the velocity pattern and thus scalar mixing is different. Analytical approaches [16,2] assume that the contributions from film and bubble caps can be calculated separately. Therefore, tracer from the film does not influence bubble caps diffusion. However, this assumption overpredicts mass transfer for a number of experiments [16]. This happens since some tracer concentration from the film is mixed with the slug and increases the overall concentration in the slug, thereby decreasing the mass transfer from the bubble caps. Therefore, the analytical estimates for the mass transfer coefficient calculation do not account for mutual mass transfer from neighboring bubbles.

Overall, mixing patterns of the film and liquid slugs are of great importance for the estimation of mass transfer [7]. However, the assumptions usually taken for mass transfer calculations are small capillary numbers and certain mixing patterns such as to help to estimate the mass transfer using the penetration theory of Higbie [17].

In comparison with analytical calculations and simplifications, the numerical approach can take into account the complex mixing patterns and geometries. However, there are challenges as to how to mimic the continuous picture where the medium is moving with bulk velocity $U = U_{\text{gas}} + U_{\text{liq}}$ as it is done in experiments. Thus, the questions indicated in Section 1 arise. The next section gives more details about numerical simulations.

2.3. Numerical simulations

Ideally one wants to mimic the continuous picture as it is seen in experiments. Thus, mass transfer simulations for a number of unit cells each containing a bubble are needed. As was indicated above, there are two approaches towards it – either to simulate the bubble train and then to measure concentration along the pipe, Eq. (10), or to transfer to the reference frame moving with the bulk velocity U and conduct the same measurements. However, both methods require tracking of moving bubbles which is complicated from the numerical point of view. Therefore, one needs to come up with a simple and smaller domain for calculations of the mass transfer coefficient, which closely mimics the continuous picture of a large number of separated bubbles.

To avoid complications with moving grids, our approach is to simulate mass transfer in a reference frame moving with the bubble. Therefore, one needs to examine Eq. (10) more closely.

We perform simulations in the frame co-moving with the bubble in which the bubble position stays constant. The bubble velocity U_{bubble} is different from the bulk velocity $U = U_{\text{gas}} + U_{\text{liq}}$, and one thus needs to perform a x coordinate variable change:

$$\begin{aligned} x(t) &= U_{\text{bubble}} t, \\ \overline{C(x)} &= C^* \left(1 - \exp\left(-k_L a \frac{x}{U_{\text{gas}} + U_{\text{liq}}}\right) \right), \\ \langle C(t) \rangle &= C^* \left(1 - \exp\left(-k_L a t \frac{U_{\text{bubble}}}{U_{\text{gas}} + U_{\text{liq}}}\right) \right), \end{aligned} \quad (11)$$

where $\langle C(t) \rangle$ is the space-averaged characteristic concentration, and $\overline{C(x)}$ is the time-averaged concentration at location x . One can make different choices for $\langle C(t) \rangle$ such as the concentration averaged over the whole domain or inlet/outlet space-averaged concentrations as used in [2,3]. The volumetric mass transfer coefficient can be obtained through the space-averaged concentration:

$$\begin{aligned} k_L a t \frac{U_{\text{bubble}}}{U_{\text{gas}} + U_{\text{liq}}} &= \ln \frac{C^*}{C^* - \langle C(t) \rangle}, \\ k_L a \frac{L_{\text{unit}}}{U_{\text{liq}} + U_{\text{gas}}} &= \frac{L_{\text{unit}}}{U_{\text{bubble}} t} \ln \frac{C^*}{C^* - \langle C(t) \rangle}, \end{aligned} \quad (12)$$

where the parameter $k_L a \frac{L_{\text{unit}}}{U_{\text{gas}} + U_{\text{liq}}}$ is non-dimensional. One can also measure the volumetric mass transfer coefficient from concentrations given at times t_1 and t_2 :

$$k_L a \frac{L_{\text{unit}}}{U_{\text{liq}} + U_{\text{gas}}} = \frac{L_{\text{unit}}}{U_{\text{bubble}}(t_2 - t_1)} \ln \frac{C^* - \langle C(t_1) \rangle}{C^* - \langle C(t_2) \rangle}. \quad (13)$$

Expressions (11)–(13) are the cornerstones of the present work. Four possible scenarios of numerical simulations have been examined:

1. One unit cell is simulated with periodic boundary conditions, see Fig. 3. In this case no tracer leaves the domain similarly to plug flow. Though easier to implement, it gives rise to the criticism that the inlet concentration is equal to the outlet one. As was discussed, in experiments there is a concentration difference between the inlet and the outlet, even for one unit cell. In this case, the volumetric mass transfer coefficient is calculated

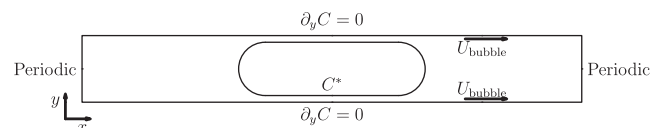


Fig. 3. The two-dimensional benchmark for the the mass transfer coefficient for the bubble located at the middle of the domain.

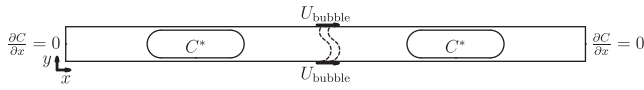


Fig. 4. Benchmark for multiple unit cells.

by Eq. (12). The characteristic concentration $\langle C(t) \rangle$ required for the volumetric mass transfer coefficient is taken as the average concentration in the domain:

$$C(t) = \frac{\int_{\text{liquid}} C dV}{\int dV}. \quad (14)$$

2. Periodic boundary conditions are applied as in the first case but the characteristic concentration is taken as the inlet/outlet flux-averaged concentration [2]:

$$\begin{aligned} \langle C_{\text{inlet}}(t) \rangle &= \frac{\int U(y)C(0, y, t) dy}{\int U(0, y) dy}, \\ \langle C_{\text{outlet}}(t) \rangle &= \frac{\int U(y)C(L_{\text{unit}}, y, t) dy}{\int U(L_{\text{unit}}, y) dy}, \end{aligned} \quad (15)$$

$$C_{\text{inlet}}(\mathbf{x}, t) = C_{\text{outlet}}(\mathbf{x}, t), \text{ due to periodicity.}$$

The assumptions of this approach are that the concentration difference between the inlet/outlet- and the space-averaged over the whole unit cell is not significant. Thus, the tracer is assumed to be well mixed in the slug.

3. The approach of van Baten and Krishna [2], where periodic boundary conditions are used and the mass transfer coefficient is calculated as the gain of the mass in the system divided by the concentration difference multiplied by the surface area:

$$k_L a = \frac{\dot{m} P}{P \Delta C V} = \frac{\dot{m}}{V(C^* - \langle C(t) \rangle)}, \quad (16)$$

where the mass flux in the domain can be calculated as:

$$\dot{m} = \frac{m_2 - m_1}{t_2 - t_1} = \frac{\int_{\text{liq}} C(\mathbf{x}, t_2) d\mathbf{x} - \int_{\text{liq}} C(\mathbf{x}, t_1) d\mathbf{x}}{t_2 - t_1}. \quad (17)$$

In the approach of van Baten and Krishna the inlet/outlet flux-averaged concentrations were taken as the characteristic concentration $\langle C(t) \rangle$.

4. Simulation of several unit cells, see Fig. 4. This situation corresponds to the head of the bubble train, after injection in the pipe and traveling along the channel. One can see that this situation best resembles the experimental picture, but also requires larger computational resources. By simulating a certain number of bubbles in the train head, the influence of the boundaries can be reduced. For example, left and right boundary conditions in this case are taken as open boundaries, i.e. $\partial C / \partial x = 0$. There is no ambiguity in the choice of the characteristic concentration. The average concentration of any unit cell far away from boundaries will be governed by Eq. (13).

One can notice that all examined cases are the extreme limits of one equation:

$$k_L a = \frac{\dot{m} - \int C_{\text{outlet}}(t) u(L_{\text{unit}}, y) dy + \int C_{\text{inlet}}(t) u(0, y) dy}{V \Delta C}, \quad (18)$$

where $\Delta C = C^* - \langle C(t) \rangle$ with $\langle C(t) \rangle$ taken to be the average concentration in the whole liquid domain, \dot{m} is the mass gain in the domain, $\int C_{\text{inlet}} u(0, y) dy$ and $\int C_{\text{outlet}} u(L_{\text{unit}}, y) dy$ are inlet/outlet mass fluxes. Eq. (18) describes the mass balance: whatever was generated by the bubble surface equals the domain mass change minus whatever left the domain plus whatever entered it.

With periodic boundary conditions:

$$\int C_{\text{outlet}}(t) u(L_{\text{unit}}, y) dy = \int C_{\text{inlet}}(t) u(0, y) dy.$$

In this case, Eq. (18) reduces to Eq. (16).

Another limiting case (will be shown later) is when the mass accumulation rate equals zero, i.e. $\dot{m} = 0$. This situation corresponds to a simulation of a few unit cells with open boundary for flows with $Ca > 0.7$.

Before we examine all the test cases above, some lattice Boltzmann mass transfer benchmarks will be presented.

3. Validation

As was discussed earlier, analytical correlations for the mass transfer coefficient have been derived for a Taylor bubble train flow as two separate contributions: the mass transfer from two half circles and the mass transfer from the film. We will examine these mass transfer cases closely with the help of the lattice Boltzmann method and compare them against analytical solutions. The next sections will give a short introduction to the lattice Boltzmann method and present benchmark results.

3.1. TRT D2Q9 model

The lattice Boltzmann equation (LBE) operates on a square/cubic grid representing the physical domain in non-dimensional terms (hereafter we use subscript LB to denote non-dimensional quantities). It utilizes probability distribution functions (also known as particle populations) containing information about macroscopic variables, such as fluid density and momentum. The LBE consists of two parts: a local collision step, and a propagation step which transports information from one node to another along directions specified by a discrete velocity set. The LBE is typically implemented as follows:

$$\begin{aligned} f_i^*(\mathbf{x}, t) &= f_i(\mathbf{x}, t) - \omega(f_i(\mathbf{x}, t) - eq_i(\mathbf{x}, t)), & \text{collision step,} \\ f_i(\mathbf{x} + \mathbf{c}_i, t + 1) &= f_i^*(\mathbf{x}, t), & \text{propagation step,} \end{aligned} \quad (19)$$

where f_i is the probability distribution function in the direction \mathbf{c}_i , eq_i is the equilibrium probability distribution function, and ω is the relaxation parameter. The term $-\omega(f_i - eq_i)$ is the so-called BGK collision operator [37]. However, the approach used here is the TRT (two-relaxation-times) collision operator [32,34]. In comparison with the widely used BGK collision operator, the TRT collision operator has better accuracy for diffusion and convection fluxes, as well as a larger range of parameters where the scheme is stable.

The TRT collision operator [38] decomposes the populations and the equilibrium distribution into a symmetric and an antisymmetric part:

$$f_i^\pm = \frac{f_i \pm \bar{f}_i}{2}, \quad eq_i^\pm = \frac{eq_i \pm eq_{\bar{i}}}{2}, \quad (20)$$

where \bar{i} is the direction opposite to the i th direction. The collision is performed with two independent relaxation rates for symmetric and antisymmetric modes:

$$\begin{aligned} f_i^*(\mathbf{x}, t) &= f_i(\mathbf{x}, t) - \omega_+(f_i^+ - eq_i^+) - \omega_-(f_i^- - eq_i^-), \\ f_i(\mathbf{x} + \mathbf{c}_i, t + 1) &= f_i^*(\mathbf{x}, t). \end{aligned} \quad (21)$$

Note that the TRT collision operator reduces to the BGK operator if $\omega_+ = \omega_-$. In comparison with the BGK collision operator, the TRT collision operator has one additional degree of freedom. The TRT operator introduces the following free parameter $A = \left(\frac{1}{\omega_+} - \frac{1}{2}\right) \left(\frac{1}{\omega_-} - \frac{1}{2}\right)$. This free parameter controls the effective location of bounce-back walls [39], second-order accuracy of the boundary [38] and interface schemes [40], spatial accuracy [41,42], consistency [43] and, to some extent, stability [44,45,42]. In particular, $A = \frac{1}{4}$ achieves the optimal stability for the isotropic advection-diffusion equation [44].

The parameters ω_+ , ω_- and eq_i fully define the lattice Boltzmann procedure. The two-dimensional, nine-velocity LBM *D2Q9* we used in this work is defined on the set of lattice velocities with components:

$$\begin{aligned} c_{ix} &= \{0, 1, 0, -1, 0, 1, -1, -1, 1\}, & \text{for } i = 0 \dots 8, \\ c_{iy} &= \{0, 0, 1, 0, -1, 1, 1, -1, -1\}, & \text{for } i = 0 \dots 8. \end{aligned} \quad (22)$$

The equilibrium functions for the *D2Q9* TRT model are represented as [44]:

$$\begin{aligned} eq_i^+ &= eq_i^{(m)} + g^{(u)} eq_i^{(u)}, \\ eq_i^{(m)} &= t_i^{(m)} c_e + eq_i^{(a)}, \\ eq_i^{(u)} &= t_i^{(u)} \frac{u_{LB,x}^2 + u_{LB,y}^2}{2} + \frac{u_{LB,x}^2 - u_{LB,y}^2}{4} p_i^{(xx)} + g_{xy}^{(u)} \frac{u_{LB,x} u_{LB,y}}{4} p_i^{(xy)}, \\ eq_i^{(a)} &= \frac{K_{LB,xx} - K_{LB,yy}}{4} p_i^{(xx)} + \frac{K_{LB,xy}}{4} p_i^{(xy)}, \\ eq_i^- &= t_i^{(a)} u_{LB,\alpha} c_{i\alpha}, \end{aligned} \quad (23)$$

where $K_{LB,xx,yy,xy}$ are proportional to components of the diffusion tensor, $c_e = \frac{K_{LB,xx} + K_{LB,yy}}{2}$, parameters $g^{(u)}$ and $g_{xy}^{(u)}$ are either zero or one (see below), and the tensor $p_i^{(xx)} = c_{ix}^2 - c_{iy}^2$, the tensor $p_i^{(xy)} = c_{ix} c_{iy}$, the weights $t_i^{(u,m,a)}$ can be chosen based on stability criteria. The most commonly used set of weights, the so-called ‘‘hydrodynamic’’ weights, were chosen:

$$t_i^{(u)} = t_i^{(m)} = t_i^{(a)} = \left\{ 0, \frac{1}{3}, \frac{1}{3}, \frac{1}{3}, \frac{1}{3}, \frac{1}{12}, \frac{1}{12}, \frac{1}{12}, \frac{1}{12} \right\}. \quad (24)$$

It can be shown through the Chapman-Enskog procedure [46], that the simple update rule with the equilibrium function presented above restores the anisotropic advection-diffusion equation:

$$\partial_t C_{LB} + \partial_\alpha C_{LB} u_{LB,\alpha} = \partial_{\alpha\beta} D_{LB,\alpha\beta} C_{LB}, \quad (25)$$

where the concentration $C_{LB} = \sum_i f_i$, and $D_{LB,\alpha\beta} = \left(\frac{1}{\omega_-} - \frac{1}{2} \right) K_{LB,\alpha\beta}$ is the following diffusion tensor:

$$D_{LB,\alpha\beta} = \begin{pmatrix} D_{LB,xx} + \left(\frac{1}{\omega_-} - \frac{1}{2} \right) (g^{(u)} - 1) u_{LB,x}^2 & D_{LB,xy} + \left(\frac{1}{\omega_-} - \frac{1}{2} \right) (g_{xy}^{(u)} - 1) u_{LB,x} u_{LB,y} \\ D_{LB,xy} + \left(\frac{1}{\omega_-} - \frac{1}{2} \right) (g_{xy}^{(u)} - 1) u_{LB,x} u_{LB,y} & D_{LB,yy} + \left(\frac{1}{\omega_-} - \frac{1}{2} \right) (g^{(u)} - 1) u_{LB,y}^2 \end{pmatrix}. \quad (26)$$

We want to resolve the isotropic advection-diffusion equation, $D_{LB} = D_{LB,xx} = D_{LB,yy}$ or $K_{LB} = K_{LB,xx} = K_{LB,yy}$, with the non-diagonal diffusion tensor components set to zero ($D_{LB,xy} = 0$). In contrast to the *D2Q5* model, with *D2Q9* it is possible to cancel the numerical diffusion by the proper choice of the equilibrium functions, i.e. $g_{xy}^{(u)} = g^{(u)} = 1$. The particular choice of parameters used in simulations is $c_e = \frac{1}{3}$, $A = \frac{1}{4}$. Thus, the diffusion coefficient in the lattice Boltzmann system D_{LB} is matched through ω_- , i.e. $D_{LB} = c_e \left(\frac{1}{\omega_-} - \frac{1}{2} \right) = \frac{1}{3} \left(\frac{1}{\omega_-} - \frac{1}{2} \right)$. For the particular choice $A = \frac{1}{4}$, ω_+ can be found easily as $\omega_+ = 2 - \omega_-$.

We validated two types of boundary conditions: Inamuro boundary conditions [35] and pressure anti bounce-back boundary conditions [39]. However, the simulation results are presented only for pressure anti bounce-back due to their ability to handle complex boundaries in a simple way:

$$f_{B,i}^* = -f_{F,i}^* + 2eq_i^+(C^*, \mathbf{u}_{LB}), \quad (27)$$

where C^* is the concentration to be imposed at the surface, \mathbf{u}_{LB} is the surface velocity, i is the direction number pointing to the domain located at the boundary surface B , \bar{i} is the direction number opposite to i and is located at the fluid node F specifically so that node B is located at the location $F + \mathbf{c}_i$.

Note that the parameters of the lattice Boltzmann scheme are connected with physical parameters only through non-dimensional numbers governing the physics of the problem. In our case,

this is the Peclet number, $Pe = \frac{U_{\text{bubble}} L}{D}$. Therefore, one can choose any quantity, for example U_{bubble} in the lattice Boltzmann units ($u_{LB,\text{bubble}}$) as long as the Peclet number is matched in physical space and numerical simulations. The fact that $u_{LB,\text{bubble}}$ can be varied in certain ranges is extremely useful in the context of numerical simulations. This allows to increase the time step and decrease the computational demand (by an order of magnitude). This point will be used in the simulations and covered later.

The next section will cover LBM benchmarks that resemble the mass transfer from a bubble (mass transfer to the liquid with the parabolic velocity profile and mass transfer from a cylinder). As soon as we move to numerical simulations, all quantities are non-dimensional. Thus, we drop the subscript *LB* for brevity.

3.2. The radial case

The case to be examined is the mass transfer from a circle with radius a , with the circle approximated as a stair-case. It can be described by the following system of equations:

$$\begin{aligned} \partial_t C(r, t) &= \frac{1}{r} \partial_r r \partial_r C(r, t), \\ C(a, t) &= C_0, \quad C(r, 0) = C_{\text{init}}. \end{aligned} \quad (28)$$

The analytical solution is [47]:

$$\frac{C(r, t) - C_0}{C_{\text{init}} - C_0} = \sum_{n=1}^{\infty} \frac{2}{\mu_n J_1(\mu_n)} \exp\left(-\mu_n^2 \frac{Dt}{a^2}\right) J_0\left(\mu_n \frac{r}{a}\right), \quad (29)$$

where μ_n is the n th zero root of the 0th order Bessel polynomial $J_0(\mu_n) = 0$. Some of the corresponding roots are as follows: $\mu_1 = 2.4048$, $\mu_2 = 5.5201$, $\mu_3 = 8.6537$, $\mu_4 = 11.7915$, $\mu_5 = 14.9309$. By taking the initial concentration as 0, one obtains:

$$C(r, t) = C_0 \left(1 - \sum_{n=1}^{\infty} \frac{2}{\mu_n J_1(\mu_n)} \exp\left(-\mu_n^2 \frac{Dt}{a^2}\right) J_0\left(\mu_n \frac{r}{a}\right) \right). \quad (30)$$

Time dependency goes via the non-dimensional time: $\tau = \frac{Dt}{a^2}$. The domain size was 129×129 with the circle radius $a = 40$ lattice units. Some results for different diffusion coefficients are presented in Fig. 5. The numerical simulations with the bounce-back boundary conditions are able to accurately reproduce the analytical results.

3.3. Poiseuille velocity profile

The problem we want to address can be formulated through the following PDE:

$$\begin{aligned} \frac{\partial C}{\partial x} U(y) &= D \frac{\partial^2 C}{\partial y^2}, \\ C(0, y) &= 0, \quad C(x, \pm\delta) = C^*, \quad \frac{\partial C}{\partial y}(x, 0) = 0, \end{aligned} \quad (31)$$

$$U(y) = U_0 \left(1 - \left(\frac{y}{\delta} \right)^2 \right).$$

The procedure to solve this problem is presented in Appendix A which yields the final solution as:

$$C = C^* - C^* \sum_{m=0}^{\infty} C_m e^{-m^4 \frac{x}{4\delta}} e^{-m^2 y^2 / (2\delta^2)} {}_1F_1\left(-\frac{m^2}{4} + \frac{1}{4}, \frac{1}{2}, m^2 \frac{y^2}{\delta^2}\right), \quad (32)$$

where coefficients C_m are taken from Eq. (A.10). The comparison between contours of analytical and simulation results is presented in Fig. 6. Parameters were taken as: $D = 0.0185$, the grid dimension is 80×1600 . The centerline velocity is $U_0 = 0.05$ which yields the Peclet number $Pe = U_0 \delta / (2D) = 108.108$. The results are in good agreement. The simulations capture accurately the singular derivative for $x = 0$.

Now that the LBM is validated against the benchmarks relevant for the flow around bubbles, one can examine the cases mentioned

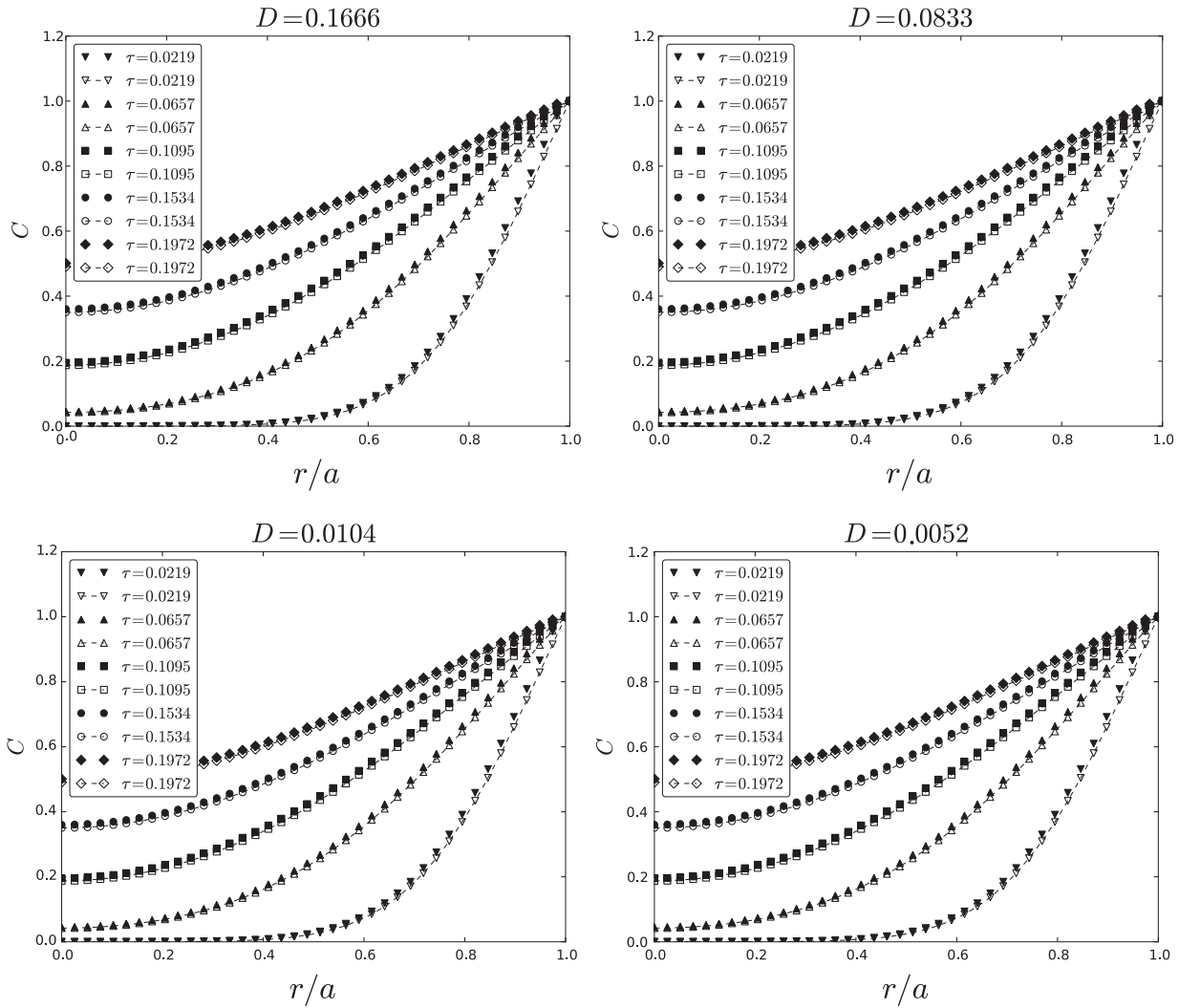


Fig. 5. Profiles for different diffusion parameters varied with ω_- (lines: Eq. (30), symbols: LB results). One can see that the diffusion from curved boundaries is captured accurately. r is the distance from the center.

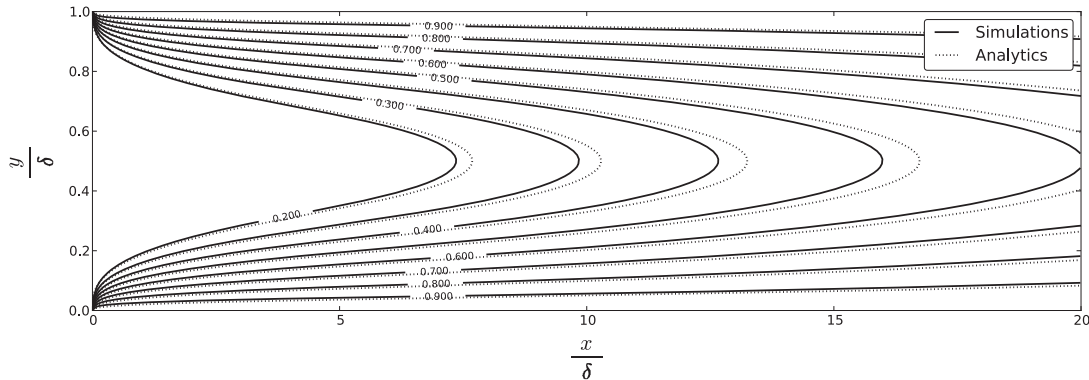


Fig. 6. Comparison between the analytical concentration contours and simulations with pressure anti bounce-back conditions, Eq. (27). The simulation was done for $D_{LB} = 0.0185$ with a 80×1600 grid. The centerline velocity is $U_0 = 0.05$, and the Peclet number is 108.108.

in Section 2.3 to calculate the volumetric mass transfer coefficient for the Taylor bubble train flow.

4. Numerical approach

A multiphase code was utilized to obtain the flow patterns and bubble shapes for different capillary numbers [18]. Five particular

cases were chosen to be examined, their results are summarized in Table 1. Note that the velocities (LB system) in Table 1 are small. This means that to match large Peclet numbers, $Pe = \frac{U_{bubble} L}{D}$, usually used in experiments, one needs to decrease the diffusion coefficient $D = \frac{1}{3} \left(\frac{1}{\omega_-} - \frac{1}{2} \right)$. Thus, the parameter $\omega_- \approx 0.5$. However, for such values of ω_- the stability of the lattice Boltzmann method

Table 1

Sample results with the binary liquid lattice Boltzmann model [18]. The following notations are used: the capillary number $Ca = \frac{U_{\text{bubble}} L}{\sigma}$, U_{liq} is the superficial liquid velocity, U_{gas} is the superficial gas velocity, ϵ_{gas} is the gas holdup, δ is the non-dimensional film thickness, L_{bubble} and L_{slug} are the non-dimensional bubble and slug lengths (defined as multiplies of the channel height). The simulation sketch is presented in Fig. 1.

Ca	Re	U_{bubble}	δ	ϵ_{gas}	U_{liq}	U_{gas}	L_{bubble}	L_{slug}
0.097	1.656	0.0055	0.092	0.30	0.0046	0.0016	5.79	9.21
0.254	4.318	0.0143	0.132	0.28	0.0108	0.0041	6.12	8.88
0.526	8.938	0.0297	0.157	0.27	0.0209	0.0080	6.19	8.81
0.750	12.744	0.0424	0.167	0.25	0.0293	0.0107	5.96	9.04
1.040	17.665	0.0588	0.177	0.22	0.0397	0.0135	5.59	9.41

drastically decreases [45]. On the other hand, one iteration in the lattice Boltzmann system corresponds to a physical time step $\Delta t_{\text{phys}} = U_{\text{bubble, LB}} \frac{\Delta x}{U_{\text{bubble, phys}}}$, where $U_{\text{bubble, phys}}$ is the physical velocity [m s^{-1}], and t_{phys} is the physical time step [s]. The iteration time is proportional to the velocity U_{LB} and the typical number of simulation steps to obtain the steady-state mass transfer coefficient for $Ca < 0.2$ is of the order of a few million. Therefore, it is desirable to increase U_{LB} while maintaining the Peclet number. If one increases the velocity, then ω_- increases as well, which impacts positively on the stability of the LBM.

Given all the considerations above, mass transfer simulations are performed as follows:

Flow field: Given a capillary number Ca , one needs to obtain hydrodynamic fields around the bubble using the multiphase binary liquid lattice Boltzmann model according to our previous work [18]. Periodic boundary conditions were used in that work. The grid used was 202×3000 which corresponds to the fluid domain of size 200×3000 . That grid resolution was taken to ensure grid independency of the results [18]. Note that we do not approximate bubble shapes by correlations, but directly resolve them using the multiphase solver.

Bubble reference frame: Once the hydrodynamics is solved, the mass transfer simulations are conducted in the reference frame moving with the bubble, where the bubble stands still and the liquid flows around the bubble. We impose a uniform and steady concentration on the surface of the bubble with the anti bounce-back condition, Eq. (27).

Velocity improvement: One can scale the velocity to perform faster simulations. However, before doing it one needs to improve the velocity field. This issue arises because of the multiphase model used in the flow simulations. The binary liquid lattice Boltzmann model is a diffuse interface model where no clear boundary between gas and liquid exists. We obtain the bubble shape by imposing a condition on the order parameter field ϕ with $\phi \leq 0$ in the bubble [18]. The velocity of the bubble is defined as the bubble tip velocity. Because of the square grid, the shape of the bubble is determined within an accuracy of one grid spacing. Thus, there is an error in the determination of the bubble velocity. Though these errors are small, there is still a small non-zero velocity component pointing into the bubble in some places, see Fig. 8 in [18] where some streamlines are penetrating the bubble surface. This small velocity is amplified upon the velocity scaling and is inconsistent with the advection-diffusion equation leading to instability after many iterations.

Thus, before performing the mass transfer simulations an additional single phase hydrodynamic simulation is performed. A free-surface solver was developed in order to obtain a velocity field consistent with the advection-diffusion equation. We take results from the multiphase simulations, extract a bubble shape using the phase indicator $\phi \leq 0$, and approximate the bubble

shape by the stair-case line with imposed free-slip boundary condition on it. The bubble velocity is then imposed on the walls. This corresponds to conducting simulations in the reference frame moving with the bubble. Appendix B covers the simple free-slip boundary condition implementation drastically improving velocity patterns. The system is iterated until a steady state is reached and as a result, all non-zero velocity components perpendicular to the bubble surface are completely eliminated. Note, that these types of simulations are much faster than the original multiphase simulations. We compared original multiphase simulations with one-component free-slip simulations. All quantities such as superficial slug and liquid velocities are within 3% for all capillary numbers in the range $0.05 \leq Ca \leq 1.0$. One can see in Fig. 7 two streamline profiles for $Ca = 0.097$ and $Ca = 1.040$.

Mass transfer: After the improved velocity profiles are obtained one can perform any mass transfer simulation with the various boundary conditions as covered in Section 2.3. For this purpose one needs to match the Peclet number Pe taken from experiments.

5. Results

This section covers simulation results. We first examine the possibility to increase the fluid velocity while keeping the Peclet number the same. After that the results for periodic boundary conditions for 5 capillary number cases will be presented. Finally, we will examine many cell simulations for two representative velocity patterns related to $Ca = 0.0907$ and $Ca = 1.04$ respectively (see Fig. 7).

The simulations were performed using an in-house code with different modifications for different boundary conditions. A typical mass transfer simulation (domain size is 3000×202 cells) for 10^6 iterations takes around 24 h on an Intel dual core CPU with the internal clock frequency of 2 GHz. All simulations (serial for one unit cell and parallel for a few unit cells) are done using computers of the WestGRID high-performance clusters in Western Canada.

5.1. Velocity scaling at constant Peclet number

This section addresses the process of significantly increasing the velocity magnitude while keeping dimensionless parameters the same to speed up simulations. This is especially important to be

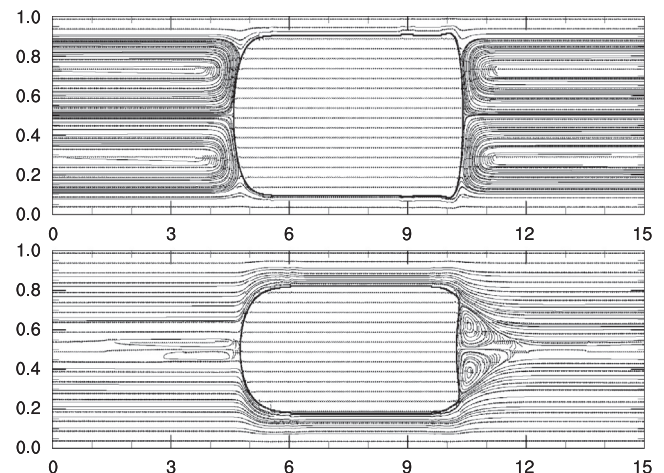


Fig. 7. The streamline patterns produced by the free-surface flow solver with simplified approximation of the free-slip bubble surface, see Appendix B. Two completely different velocity patterns are obtained, $Ca = 0.097$ (top) and $Ca = 1.040$ (bottom).

able to simulate a few unit cells in a reasonable time. For example, ten unit cell simulations require a grid of $30,000 \times 202$ nodes. Since the Peclet number is the only dimensionless quantity governing the advection-diffusion equation:

$$Pe = \frac{U_{\text{bubble}} N_y}{D} \quad (33)$$

One needs to increase the diffusion coefficient when the velocity is increased. Simulation runs were made with velocities 2, 4, 6, 8, 10, 15, 20, 40 times larger than the original velocities. The velocities, their corresponding capillary and Schmidt numbers are presented in Table 2. One can see that the Schmidt number, $Sc = Pe/Re \approx 790$, has a value corresponding to a dye with a low molecular diffusivity. This is done to minimize the dye diffusion influence on results but rather study the mass transfer in hydrodynamics patterns provided by the Taylor bubble flow. Periodic boundary conditions were used and the mass transfer coefficient was calculated according to Eq. (4). One can see in Table 2 that for small capillary numbers ($Ca < 0.2$) it is possible to scale up velocity significantly (20–40 times) to obtain a velocity around 0.2 where simulations are still stable. However, for larger capillary numbers the scale up is smaller (2–4 times), and the velocity for stable simulations is around 0.1. Table 2 shows that the velocity limit for periodic boundary conditions is 0.1 across all capillary numbers. To be on the safe side, velocities should not be scaled up beyond that value. It gives us a preliminary idea to what extent one can scale periodic mass transfer simulations. The concentration contour profiles corresponding to Table 2 for different velocity scalings are presented in Fig. 8. One can see an acceptable agreement between the cases with the same Peclet number but different velocity scalings. Note, that the speedup can be up to 10–40 times.

5.2. Average concentration results

In this section we will examine the case where the volume averaged concentration over time is used as the characteristic concentration. To calculate the volumetric mass transfer coefficient we

Table 2

Indications of the achievable stable velocity U_{bubble} when one scales velocity. Since the physical time step represented by a single iteration of the simulation is directly proportional $U_{\text{bubble,LB}}$, scaling the velocity directly translates to an effective speed-up of the simulation. Note that time iterations indicated in the table correspond to the same moment in physical time. One can see that scaling produces adequate results when C_{aver} is compared. The contour profiles for all of these cases (capillary number Ca and all scales) are presented in Fig. 8.

Scale	U_{bubble}	ω_-	Time iterations	C_{aver}
$Ca = 0.097, Pe = 1313, Sc = 792.87$				
2	0.011	1.98	400,000	0.318
4	0.023	1.96	200,000	0.319
8	0.044	1.92	100,000	0.320
10	0.055	1.90	80,000	0.321
20	0.11	1.81	40,000	0.324
40	0.22	1.66	20,000	0.328
$Ca = 0.254, Pe = 3414, Sc = 790.64$				
2	0.0286	1.98	800,000	0.6533
4	0.0572	1.96	400,000	0.6591
8	0.1144	1.92	200,000	0.6692
10	0.1430	1.90	160,000	0.6734
20	0.2860	1.81	80,000	0.6894
$Ca = 0.526, Pe = 7092, Sc = 793.46$				
2	0.0594	1.98	200,000	0.3271
4	0.1188	1.96	100,000	0.3315
$Ca = 0.750, Pe = 10,125, Sc = 794.49$				
2	0.0848	1.98	200,000	0.3489
$Ca = 1.040, Pe = 14,041, Sc = 794.84$				
2	0.1176	1.98	200,000	0.3675

used Eq. (12). Results for the coefficient $k_L a \frac{U_{\text{bubble}}}{U_{\text{gas}} + U_{\text{liq}}}$ are shown in Fig. 9 for different capillary, Peclet numbers and velocity scalings indicated in Table 2. When the average concentration gets close to $C^* = 1$, Eq. (12) gives inadequate results due to the accuracy of the logarithmic function evaluation. This is the reason that curves in Fig. 9 tend to shoot up for long times. Due to velocity scaling each simulation has a different physical time step. Thus, we normalized time such that it represents a number of unit cell lengths which the bubble has travelled, i.e. $N_{\text{cell units}} = \frac{\text{scale} \cdot U_{\text{bubble}} \cdot N_{\text{iter}}}{L_{\text{unit}}}$. Fig. 9 shows the volumetric mass transfer dependency against the distance in unit cell length. One can see in Table 3 that for different Peclet numbers different time (number of unit cells) is required to achieve steady state. For example, for larger Peclet numbers fewer length is required to achieve the steady state condition.

Overall one obtains steady state volumetric mass transfer coefficients for periodic boundaries simulations if the following conditions are fulfilled:

- I Scaling is performed so that $U_{\text{max}} = \text{scale} \cdot U_{\text{bubble}} \leq 0.1$.
- II The larger the Peclet number, the fewer iterations are required. One can extrapolate data from Table 3, say L_{steady} , and estimate the number of iterations to reach the steady-state as $\text{scale} \cdot U_{\text{bubble}} \cdot N_{\text{iter}} \leq L_{\text{steady}}$.

5.3. Periodic boundaries with the inlet/outlet characteristic concentration

The volumetric mass transfer coefficient was calculated using Eq. (12) with the characteristic concentration being the inlet/outlet flux averaged concentration as used by van Baten and Krishna [2]. One can see in Fig. 10 that the calculated volumetric mass transfer coefficient behaves differently from the domain averaged volumetric mass transfer coefficient. For example, for small capillary numbers, i.e. $Ca = 0.097, 0.254, 0.526$ the values are overpredicted ($k_L a \frac{L_{\text{unit}}}{U_{\text{liq}} + U_{\text{gas}}} = 0.3, 0.25, 0.1$). When the velocity pattern changes from having a vortex in front of the bubble to not having it, i.e. $Ca = 0.75, 1.04$ the calculated values are underpredicted compared to estimates based on volume-averaged concentration, i.e. $k_L a \frac{L_{\text{unit}}}{U_{\text{liq}} + U_{\text{gas}}} = 0.06, 0.04$. As we will see later, the domain-averaged characteristic concentration produces proper mass transfer coefficients.

5.4. Van Baten and Krishna formulation

The van Baten and Krishna [2] formulation, Eq. (16), is calculated as the change of mass in the domain divided by the time difference. We examined two approaches: the characteristic concentration taken to be as the domain average and as the flux-averaged input/output concentration. The latter case corresponds to [2]. The results are presented in Fig. 11 for $Ca = 0.097$ and $Ca = 1.04$. One can see that the inlet/outlet flux averaged concentration is inconsistent. The reason that van Baten and Krishna [2] obtained the mass transfer coefficient close to the analytical estimation is that the liquid slug is well mixed ($Ca < 0.1$ which is below the range studied here) so that the averaged concentration is close to the inlet/outlet concentration.

However, results for the domain-averaged concentration using the approach of van Baten and Krishna are close to simulation results in Section 5.2. Note that for $Ca = 0.097$ the obtained mass transfer coefficient value is 10% lower than the value in Section 5.2. However, as will be shown later the obtained volumetric mass transfer coefficient for $Ca = 0.097$ has the same value as for the simulations of a few unit cells. Therefore the approach of [2] produces accurate results if the characteristic concentration is the volume-averaged concentration (not the inlet/outlet flux-averaged concentration used in the original work). From the computational

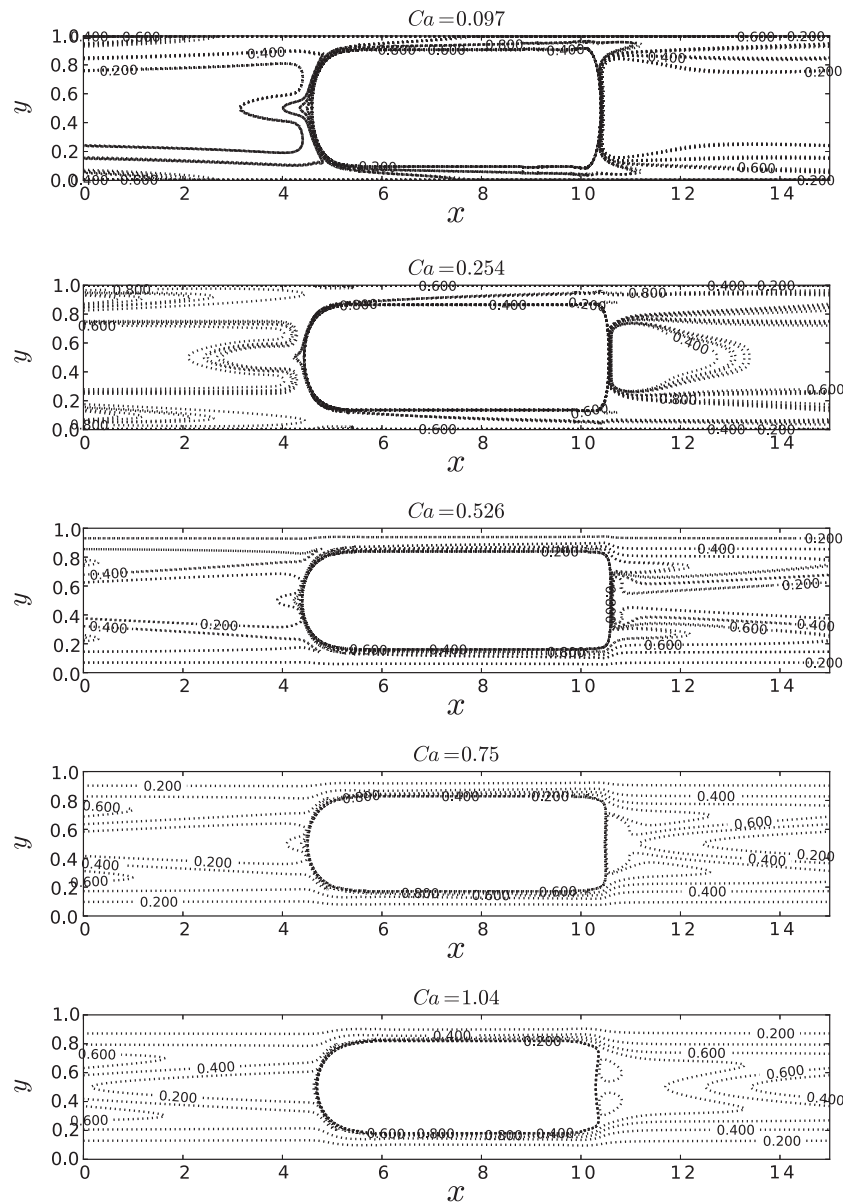


Fig. 8. Concentration contour profiles for velocity scalings as identified in Table 2 (top to bottom: $Ca = 0.097, 0.254, 0.526, 0.750, 1.040$). Lines correspond to all different scales indicated in Table 2 (top to bottom: 6 scalings, 5 scalings, 2 scalings, 1 scaling, 1 scaling). Lines for different scaling parameters coincide with or are close to each other showing that simulations with velocity scalings are consistent.

point of view, it also requires the concentration fields in time and space to calculate the mass change in time and the averaged domain characteristic concentration.

5.5. Simulations for several unit cells

In order to achieve independence from the boundary conditions and a closer match with the physical system being modeled, one can simulate several unit cells, corresponding to the head of a bubble train. If end effects are eliminated then the average domain characteristic should change in time according to Eq. (13). This eliminates the ambiguity inherent in choosing a definition of the characteristic concentration, it becomes the same domain-averaged concentration as the one measured in experiments.

This section studies the number of unit cells required for the volumetric mass transfer coefficient to be independent of the influence of boundaries. We chose two different velocity patterns (see Fig. 7 for $Ca = 0.097$ and $Ca = 1.04$) to perform the simulations.

For $Ca = 0.097$ we performed simulations with 4, 6, 8, 10 cells, and for $Ca = 1.040$ only with 4, 6, 8 cells. We observed however that simulations with a domain length of 10 unit cells produce the same results as those with 8 unit cells.

We keep velocity in the range 0.05–0.1 to avoid excessively long simulation times. The number of steps for mass to pass through the whole domain can be approximated as $1.5 \frac{L_{\text{unit}}}{U_{\text{bubble}}}$, which takes into account the bulk velocity. If U_{bubble} is taken as 0.05 then for the domain size $L_{\text{unit}} = 3000$ one can obtain the following number of iterations for the mass to cross the unit cell $1.5 \frac{3000}{0.05} = 90,000$. Therefore, 10^6 iterations are enough for a system consisting of 10 unit cells. For more accurate estimations of the number of time steps depending on the Peclet number we refer to Section 5.1.

5.6. $Ca = 0.097$ results

There are two characteristics we want to track in the simulations: the average concentration in the unit cell with time (see

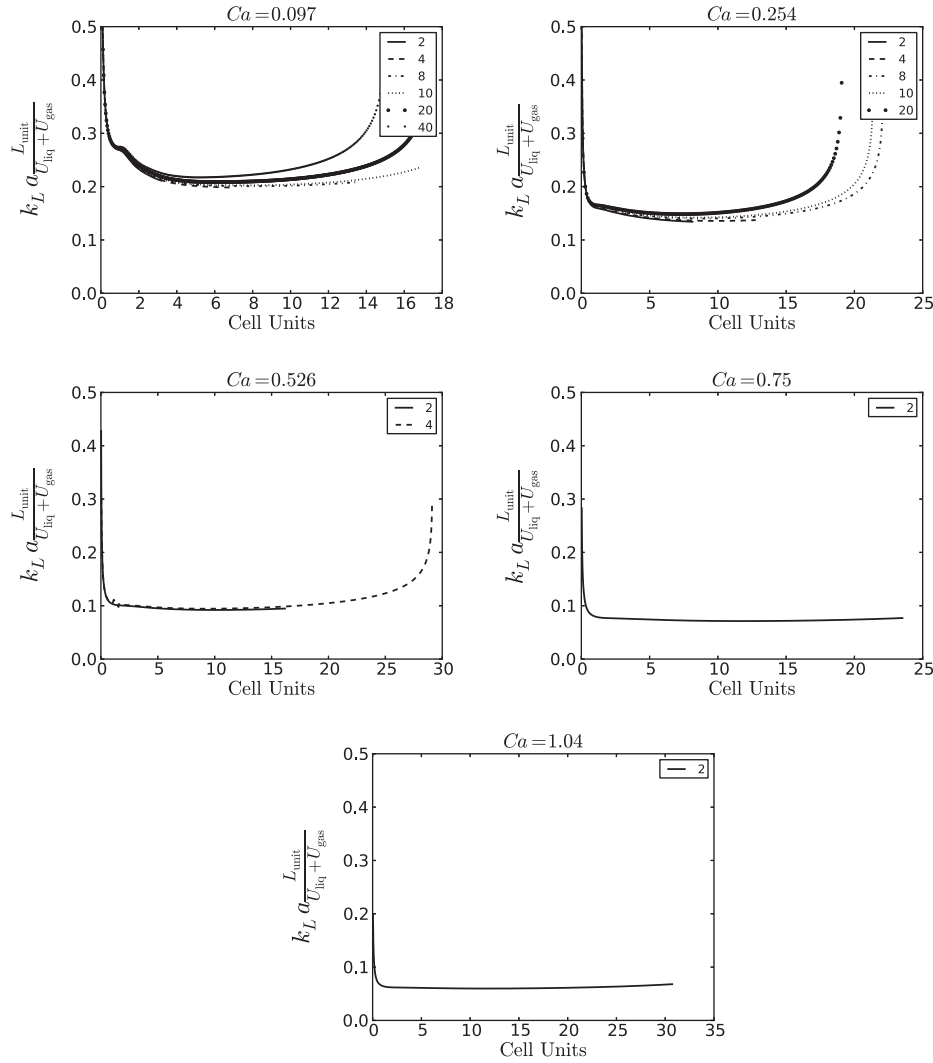


Fig. 9. Volumetric mass transfer coefficient for different capillary numbers and velocity scales against the bubble travel distance in the laboratory frame. The “Cell Units” axis refers to the physical distance in unit cells lengths the bubble travels. A legend is provided for velocity scalings. All of them show a good agreement. One can see an abnormal rise of the mass transfer coefficient when the average concentration is close to C^* due to the logarithmic function evaluation. Table 3 summarizes the results presented here.

Table 3
The distance which a bubble propagates when the steady-state condition is achieved.

Ca	Pe	$L_{\text{steady}}/L_{\text{unit}}$	$k_L a_{U_{\text{liq}}+U_{\text{gas}}}^{L_{\text{unit}}}$
0.097	1313	7	0.21
0.254	3414	6	0.14
0.526	7092	3	0.095
0.750	10,125	3	0.074
1.040	14,041	2	0.0601

Eq. (13)), and the accumulated mass rate in the domain which takes into account inlet/outlet fluxes (see Eq. (18)). The former resembles experiments: if one has a large enough number of unit cells, then the averaged domain concentration should change in time according to Eq. (13):

$$k_L a_{U_{\text{gas}}+U_{\text{liq}}}^{L_{\text{unit}}} = \frac{L_{\text{unit}}}{U_{\text{bubble}}(t_2 - t_1)} \ln \left(\frac{C^* - \langle C(t_1) \rangle}{C^* - \langle C(t_2) \rangle} \right) \quad (34)$$

The non-dimensional volumetric mass transfer coefficient calculated based on Eq. (34) (domain-averaged concentration change in time) is represented in Fig. 12 for different unit cells. One can see that mass transfer coefficient values are the same as the mass flux

concentration based on the van Baten and Krishna formulation with the characteristic concentration being the domain-averaged concentration (see Section 5.4). This demonstrates two things: the domain-averaged concentration is the only choice for the characteristic concentration, and periodic boundary conditions for one unit cell produce good results.

In comparison with periodic boundary conditions Eq. (18) allows to calculate the mass transfer coefficient differently. Eq. (18) can be rewritten as:

$$k_L a_{U_{\text{liq}}+U_{\text{gas}}}^{L_{\text{unit}}} = \frac{L_{\text{unit}}}{U_{\text{gas}}+U_{\text{bubble}}} \frac{V(C(t_2)) - (C(t_1)) - \int C_{\text{outlet}}(L_{\text{unit}}, y, t^*) u(L_{\text{unit}}, y) dy + \int C_{\text{inlet}}(0, y, t^*) u(0, y) dy}{V(C^* - \langle C(t^*) \rangle)}, \quad (35)$$

where t^* is the mean between t_1 and t_2 .

Fig. 13 shows average concentrations in different units and $k_L a_{U_{\text{liq}}+U_{\text{gas}}}^{L_{\text{unit}}}$ based on Eq. (35) calculated for each unit for velocity scale 10 and 6 unit cells (all velocity scales produce the same results). It shows that the volumetric mass transfer coefficient is consistent for internal segments, i.e. unit cells numbers 2–4. The results for the volumetric mass transfer coefficient calculated by Eq. (18) for multiple unit cells are close (less than 10% deviation) to results for periodic boundary conditions in Section 5.2. The same

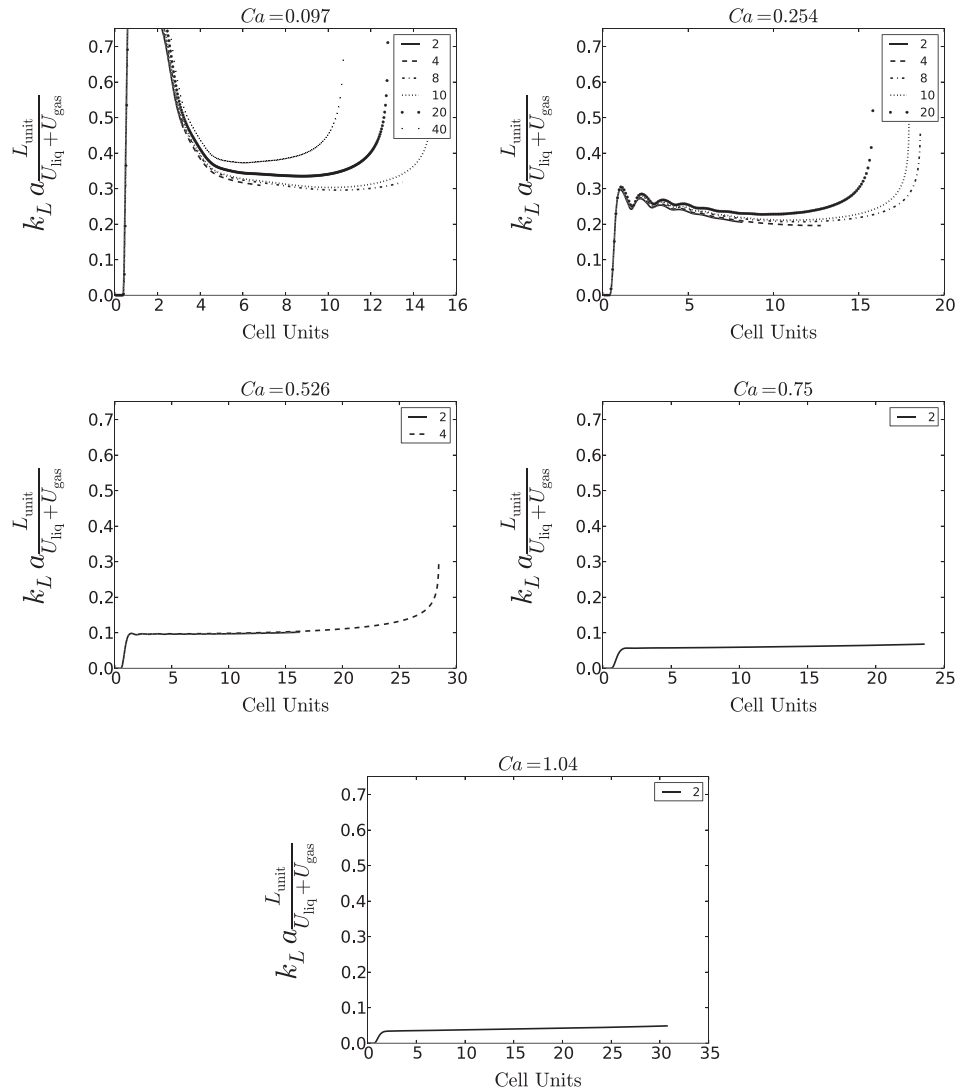


Fig. 10. The volumetric mass transfer coefficient with the characteristic concentration based on the inlet/outlet flux averaged concentration as in [2]. One can see that depending on the velocity pattern, the values are either overpredicted or underpredicted in comparison to values specified in Table 3.

dependencies can be found for 8 and 10 unit cells simulations but we do not present them here. We also do not present 4 unit cells simulation results which are highly influenced by entrance and exit effects.

The calculation of the volumetric mass transfer coefficient is more difficult using Eq. (35). However, it will be shown below that this equation can be significantly simplified in case of larger capillary numbers ($Ca > 0.7$).

5.7. $Ca = 1.040$ results

The same correlations were examined for a different velocity pattern at $Ca = 1.040$. The original Peclet number we started with is $Pe = 14,041$ (Table 2). To avoid stability problems of the lattice Boltzmann method we changed the original Peclet number by increasing diffusion to $Pe = 2644$ (corresponding Schmidt number $Sc = 709.84/5 = 158.96$). Our goal is to understand the influence of velocity pattern, not to perform simulations with a certain Peclet number. Thus, we have a certain degree of freedom to vary the simulations' Peclet number. This is achieved by adjusting velocity and diffusion coefficients. For example, if the velocity scaling is 2, then by increasing the initial diffusion coefficient 10 times one will eventually obtain a Peclet number 5 times smaller than the initial

Peclet number. The results with respect to the number of unit cells are the same as for $Ca = 0.097$: at least 6 unit cells are required to avoid the influence of inlet/outlet effects. Thus, only 6 unit cells results are presented in Fig. 14 which shows the average concentration for each unit cell. One can see that the average volume concentration for each unit cell converges to a constant value. Thus, all the mass generated by the bubble is transferred through the boundaries. This indicates that the liquid slug is unmixed since no concentration travels back to inlet with the vortex and increases the average concentration in each unit cell. Note that the periodic boundary conditions cannot show whether the liquid slug is mixed or not due to the fact that the averaged domain concentration always increases in time. Thus, the volumetric mass transfer coefficient $k_L a_{L_{unit}} / (U_{liq} + U_{gas})$ can be calculated according to the definition, Eq. (18):

$$k_L a = \frac{\dot{m} - \int C_{outlet}(y)u(L_{unit}, y)dy + \int C_{inlet}(y)u(L_{unit}, y)dy}{V(C^* - \langle C(t) \rangle)}, \quad (36)$$

where V is the unit cell volume. There is no accumulated mass in the domain, so $\dot{m} = 0$. Like periodic boundary conditions, this case is another extreme limit of Eq. (18). Note that to calculate the volumetric mass transfer coefficient one needs only the spatial information and does not require the knowledge of how the aver-

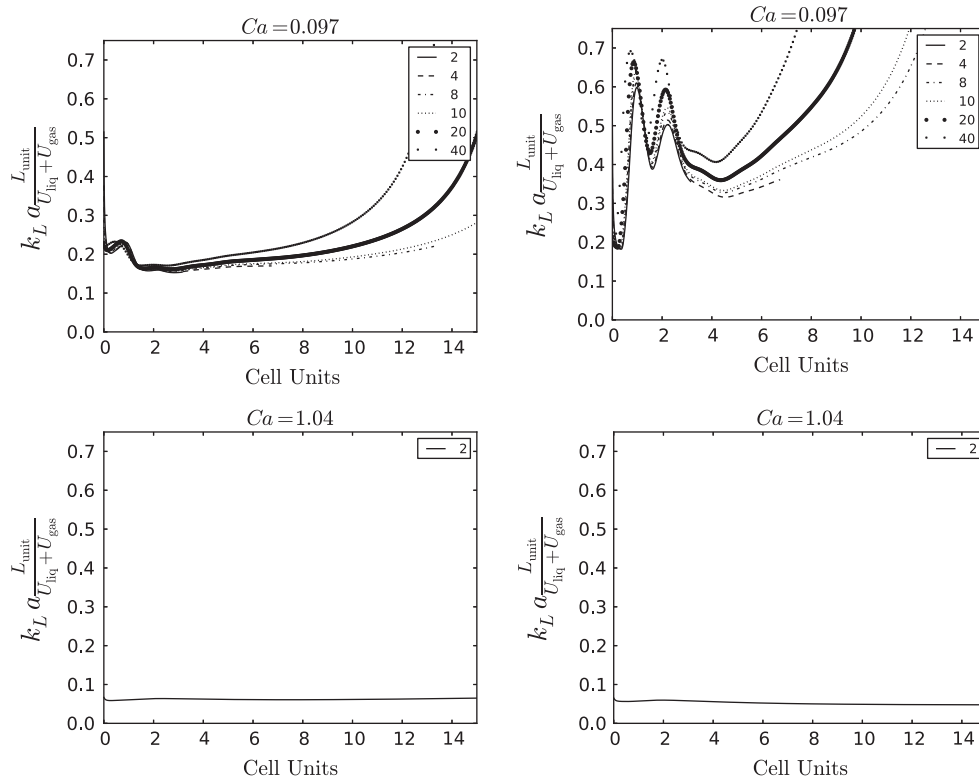


Fig. 11. The [2] formulations for $Ca = 0.097$ (top) and $Ca = 1.04$ (bottom) with the characteristic concentration being domain-averaged (left) and inlet/outlet flux-averaged (right). One can see that the [2] formulation produces good results with the characteristic concentration being the average concentration. Moreover, the values are closer to values obtained with many cell simulations, see Fig. 12, than with periodic boundary simulations in Section 5.2. The characteristic concentration being inlet/outlet flux-averaged does not produce consistent results.

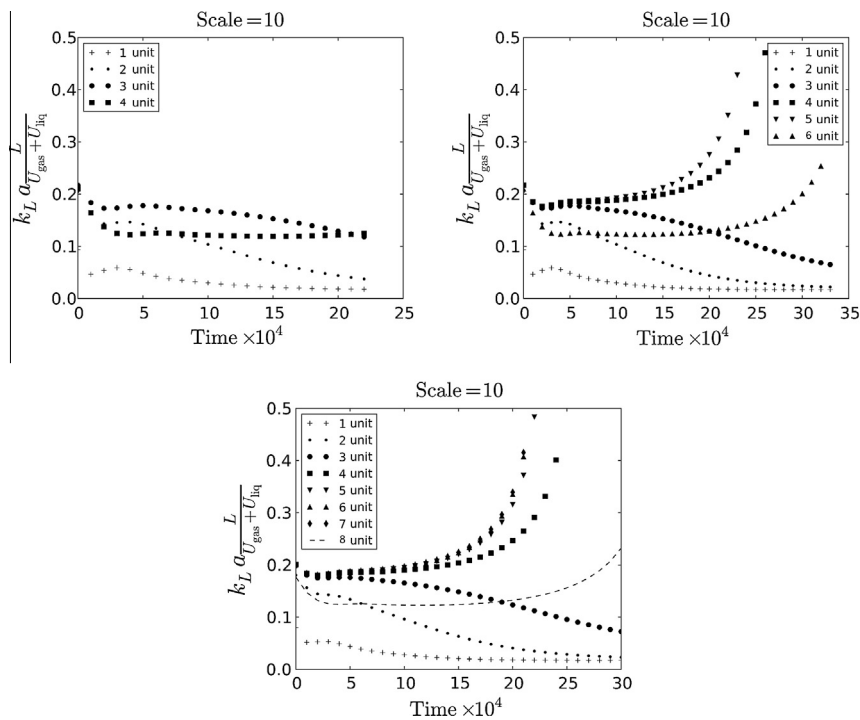


Fig. 12. The non-dimensional volumetric mass transfer coefficient defined in Eq. (34) for 4 (top left), 6 (top right), 8 unit cells (bottom). Only scale 10 is presented since all other simulations produce the same results. One can see that 4 unit cells is not enough to avoid the influence of boundaries. However, the results for 6 and 8 unit cells are consistent and show that beginning from the third unit cell and ending with the penultimate cell, the results are consistent with periodic boundary simulations and [2] formulations.

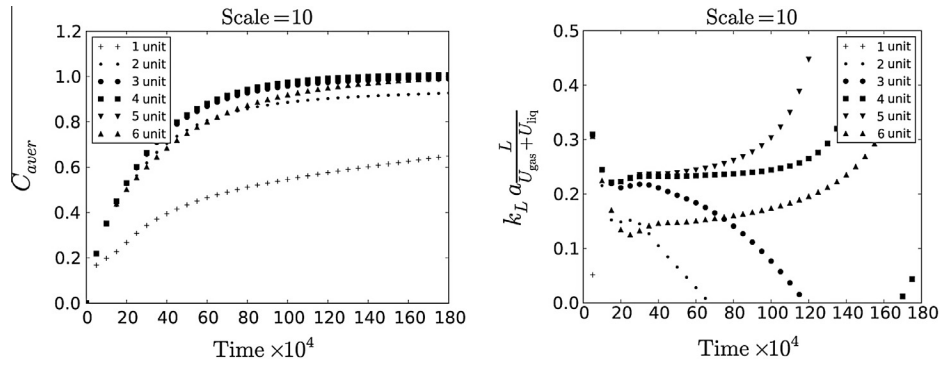


Fig. 13. Average concentrations (left) and volumetric coefficients (right) for 6 unit cells. The volumetric mass transfer coefficient is calculated based on Eq. (35) and accounts for inlet and outlet fluxes.

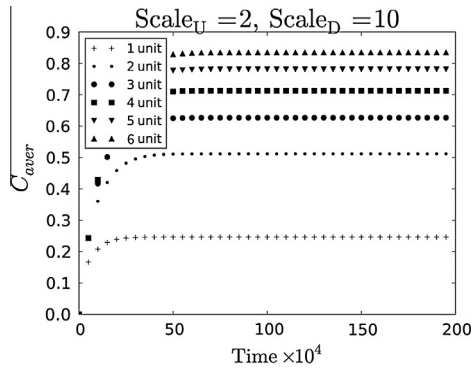


Fig. 14. Results for 6 unit cells. The Peclet number is $Pe = 2644$. One can see that the average concentrations reach a certain value and stay constant. Thus, the volumetric mass transfer coefficient, $k_L a_{\frac{L_{unit}}{U_{liq} + U_{gas}}}$, can be calculated using the spatial approach, see Fig. 15. To decrease the initial Peclet number from 14,041 to 2644, the corresponding scaling parameters for velocity and diffusion equal to 2 and 10.

aged concentration changes in time, which significantly lowers storage requirements for the simulations with $Ca > 0.7$ where there is no vortex in the liquid slug.

Fig. 15 (bottom) shows the volumetric mass transfer coefficient based on spatial calculations of inlet/outlet concentrations. One can see that the volumetric mass transfer coefficient is close to the calculated volumetric mass transfer coefficient using the time averaged approach and periodic boundaries one unit cell simulations (presented in the same figure for comparison). Note that results for approaches which incorporate the volume-averaged characteristic concentration either for one cell or a few unit cells coincide. Therefore, for certain hydrodynamic patterns ($Ca > 0.7$), one can easily convert time domain to spatial domain calculations using simulations of several unit cells.

5.8. Comparison of experimental and analytical correlations

While the goal of this paper is not to compare simulation results with the experimental measurements, we felt that a short note about such comparison will be beneficial. Unfortunately, to the authors' knowledge, there are no reported experimental results measuring the mass flux for bubbles flowing between parallel plates. However, an interesting correlation for the volumetric mass transfer coefficient was presented by Yue et al. [7] for three-dimensional microchannel geometries:

$$k_L a = \frac{2}{d_r} \left(\frac{DU_{bubble}}{L_{bubble} + L_{slug}} \right)^{0.5} \left(\frac{L_{bubble}}{L_{bubble} + L_{slug}} \right)^{0.3}, \tag{37}$$

$$k_L a \frac{L_{unit}}{U_{gas} + U_{liq}} = 2 \frac{L_{unit}}{d_r} \left(\frac{D}{L_{unit}(U_{bubble} + U_{gas})U_{gas} + U_{liq}} \right)^{0.5} \left(\frac{L_{bubble}}{L_{bubble} + L_{slug}} \right)^{0.3} \propto Pe^{-\frac{1}{2}},$$

One can see that the volumetric mass transfer correlation should be approximately proportional to $Pe^{-0.5}$. One can also use analytical estimates of the volumetric mass transfer coefficient calculated using the Higbie penetration theory [17]. One can derive the analytical expression for the mass transfer for bubble train flow between parallel plates by following the works [16,2]:

$$k_L a \frac{L_{unit}}{U_{liq} + U_{gas}} = \frac{L_{unit}}{U_{gas} + U_{liq}} \left(4 \sqrt{DU_{bubble}} \pi \frac{\sqrt{L_{bubble} - H(1 - 2\delta)}}{L_{unit}H} + 2\sqrt{2} \sqrt{DU_{bubble}} \frac{\sqrt{H(1 - 2\delta)}}{L_{unit}H} \right), \tag{38}$$

where H is the channel height, and δ is the non-dimensional film thickness (in channel heights).

Fig. 16 shows a comparison between the correlation by Yue et al. [7], the analytical expression, Eq. (38), and the current simulation results presented in Table 3. The coefficients are close to each other, especially given that the correlation by Yue et al. [7] is for three-dimensional cases. The fitting procedure based on the results of this work showed that the power of the Peclet number dependence is -0.50038 which is close to the theoretical value -0.5 . The fitting curve is $7.745 Pe^{-0.50038}$.

6. Summary

This work examines a way to calculate the volumetric mass transfer coefficient of Taylor/Batchelor bubble train flow in the framework of the lattice Boltzmann method. The volumetric mass transfer for the Taylor/Batchelor bubble train flow can be relatively easily estimated by measuring concentrations of a scalar along the streamwise direction. In comparison with the continuous nature of experiments, i.e. where one does not distinguish bubbles, the numerical simulations are performed with a small number of discrete unit cells, each containing a bubble. This work bridges the continuous nature of experiments and a few unit cells simulations performed in the reference frame moving with the bubble. We thoroughly performed and examined simulations with different definitions of the volumetric mass transfer coefficient and characteristic concentration, i.e. domain-averaged or flux-averaged inlet/outlet concentrations, for different hydrodynamic patterns seen in the bubble train flow. We also performed open inlet/outlet mass transfer simulations for a few unit cells to resemble the continuous picture seen in experiments. By thorough comparison it was shown that the easiest recipe is to perform simulations with periodic boundary conditions and calculate the volumetric mass transfer coefficient based on the domain-averaged concentration through any formulation (van Baten and Krishna, periodic boundary conditions, simulations of several unit cells) as they produce consistent

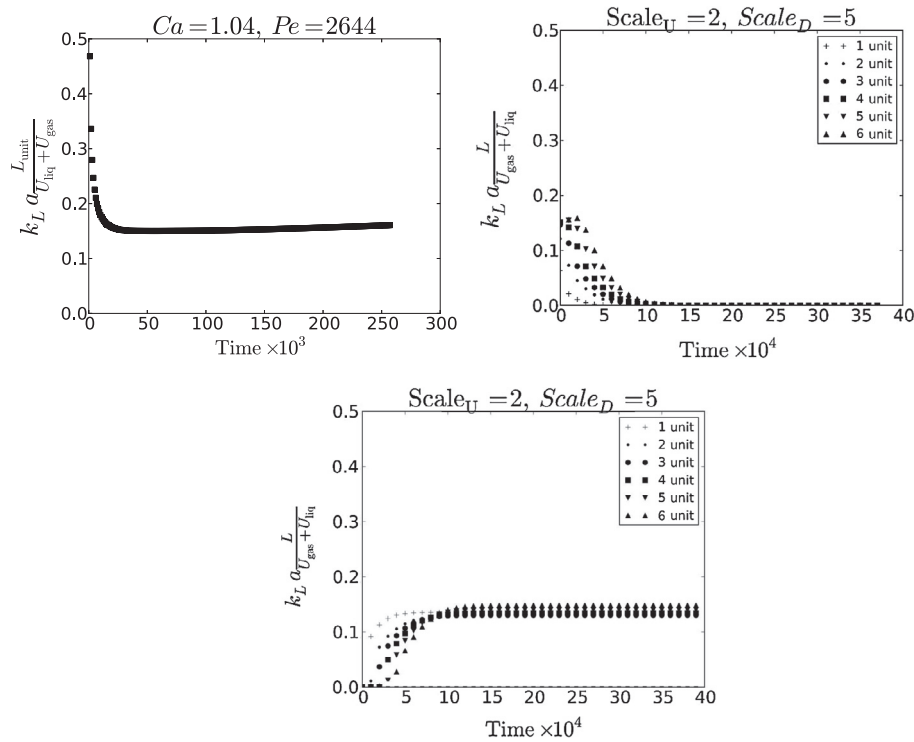


Fig. 15. The periodic (top left, 1 unit cell, Eq. (13)), unit cells domain-averaged concentrations as a function of time (top right, 6 unit cells, Eq. (13)), and spatial location (bottom, 6 unit cells, Eq. (36)) calculated volumetric mass transfer coefficients. For the upper right figure, where the time-averaged calculation is presented, one needs to consider only results where there is no concentration saturation. Thus, one needs to consider only results with less than 20,000 iterations as the saturation happens fast due to the high Peclet number. It is not convenient to use them in practical cases for unmixed slugs, i.e. $Ca > 0.7$. All results coincide and give value of around 0.15–0.16. However, the calculations based on periodic boundary conditions produce a slightly overestimated volumetric mass transfer coefficient.

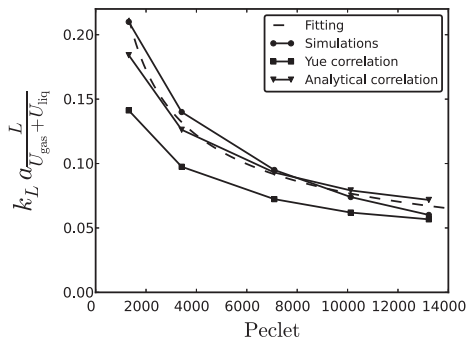


Fig. 16. Comparison between the correlation by [7], the analytical correlation derived by following the work [16] and the mass transfer coefficient based on periodic boundary conditions. The fitting curve ($7.745Pe^{-0.50038}$) is proportional to $Pe^{-0.5}$ which corresponds to all correlations. One can as well see that the deviation from the analytical expression becomes larger with the increasing Peclet number, which happens because the analytical expression does not account for the velocity pattern and the bubble shape change.

results. The best accuracy in terms of closeness to the results of simulations of several unit cells (continuous picture seen in experiments) is achieved with formulations based on the mass difference or on the domain-averaged concentrations taken in different times, Eq. (13). Eq. (11) gives a slightly overestimated volumetric mass transfer coefficients (less than 10%). The original formulation of van Baten and Krishna [2] is inconsistent if one takes the inlet/outlet flux-averaged concentration to be the characteristic concentration as in their original work. Simulations of several unit cells are harder to perform, but they provide a good reference point since they more closely resemble the continuous nature of the bubble train flow. In addition, simulations of several unit cells

indicate how well the liquid slug is mixed. This can be used for velocity patterns related to $Ca \geq 0.7$ (weak liquid slug mixing) which allows to calculate the volumetric mass transfer coefficient based on the spatial location only, without requiring the time snapshots of domain concentration values used in all other approaches. Finally, a sample of results was compared with the experimental correlation of Yue et al. [7] and shown to be consistent.

Acknowledgements

M.J. acknowledges a scholarship from the TWING project co-financed by the European Social Fund. A.K. wants to thank Schlumberger for their financial support.

Appendix A. Mass transfer for planar Poiseuille flow

Close to the previous example but with a different velocity profile, the problem can be formulated through the following PDE:

$$\begin{aligned} \frac{\partial C}{\partial x} U(y) &= D \frac{\partial^2 C}{\partial y^2}, \\ C(0, y) &= 0, \quad C(x, \pm\delta) = C^*, \quad \frac{\partial C}{\partial y}(x, 0) = 0, \\ U(y) &= U_0 \left(1 - \left(\frac{y}{\delta}\right)^2\right). \end{aligned} \quad (\text{A.1})$$

The following substitution simplifies the form of equations:

$$\begin{aligned} \zeta &= \frac{x}{\delta} \frac{D}{U_0 \delta} = \frac{1}{Pe} \frac{x}{\delta}, \\ \xi &= \frac{y}{\delta}. \end{aligned} \quad (\text{A.2})$$

Then the following equation can be obtained:

$$\frac{\partial \Theta}{\partial \zeta} (1 - \zeta^2) = \frac{\partial^2 C}{\partial \zeta^2}, \quad (\text{A.3})$$

$$\Theta(\zeta, \xi) = C - C^* \Theta(0, \xi) = -C^* \Theta(0, \pm 1) = 0.$$

After separation of variables, $\Theta(\zeta, \xi) = X(\zeta)Y(\xi)$ one can come up with two equations:

$$\frac{dX(\zeta)}{d\zeta} + m^4 X(\zeta) = 0, \quad (\text{A.4})$$

$$\frac{d^2 Y(\xi)}{d\xi^2} + m^4 (1 - \xi^2) Y(\xi) = 0.$$

The first equation has a solution:

$$X(\zeta) = \exp(-m^4 \zeta). \quad (\text{A.5})$$

The second equation can be simplified after substitution $\bar{\xi} = m\sqrt{2}\xi$ to the standard equation:

$$Y'' - \left(\frac{1}{4}\bar{\xi}^2 + a\right)Y = 0, \quad (\text{A.6})$$

where $Y' = dY/d\bar{\xi}$, and $a = -m^2/2$. The equation above has two solutions via parabolic cylinder functions or through the confluent hypergeometric function [48]:

$$Y_1 = e^{-\bar{\xi}^2/4} {}_1F_1\left(\frac{a}{2} + \frac{1}{4}, \frac{1}{2}, \frac{\bar{\xi}^2}{2}\right), \quad (\text{A.7})$$

$$Y_2 = e^{-\bar{\xi}^2/4} {}_1F_1\left(\frac{a}{2} + \frac{3}{4}, \frac{3}{2}, \frac{\bar{\xi}^2}{2}\right).$$

Taking symmetry conditions into consideration by leaving only the even solution, Eq. (A.4) has the following solution:

$$Y_m = C_m e^{-m^2 \xi^2/2} {}_1F_1\left(-\frac{m^2}{4} + \frac{1}{4}, \frac{1}{2}, m^2 \xi^2\right). \quad (\text{A.8})$$

To satisfy the boundary condition we need to find zeros of the hypergeometric function, i.e. ${}_1F_1\left(-\frac{m^2}{4} + \frac{1}{4}, \frac{1}{2}, m^2\right) = 0$. First ten eigenvalues can be found using numerical methods: 1.2967, 2.3811, 3.1093, 3.6969, 4.2032, 4.6548, 5.0662, 5.4467, 5.8023, 6.1373. One needs to satisfy one more condition to obtain coefficients C_m :

$$-C^* = \sum_m C_m e^{-m^2 \xi^2/2} {}_1F_1\left(-\frac{m^2}{4} + \frac{1}{4}, \frac{1}{2}, m^2 \xi^2\right). \quad (\text{A.9})$$

One can multiply both parts on $(1 - \xi^2) {}_1F_1\left(-\frac{m^2}{4} + \frac{1}{4}, \frac{1}{2}, m^2 \xi^2\right)$ and through orthogonality (Stourm-Liouville theorem) obtain coefficients:

$$C_m = -C^* \frac{\int_{\xi=0}^1 (1 - x^2) e^{-m^2 \xi^2/2} {}_1F_1\left(-\frac{m^2}{4} + \frac{1}{4}, \frac{1}{2}, m^2 \xi^2\right) d\xi}{\int_{\xi=0}^1 (1 - \xi^2) e^{-m^2 \xi^2/2} {}_1F_1\left(-\frac{m^2}{4} + \frac{1}{4}, \frac{1}{2}, m^2 \xi^2\right)^2 d\xi}. \quad (\text{A.10})$$

Therefore the complete solution can be written as:

$$C = C^* - C^* \sum_{m=0} C_m e^{-m^4 \frac{x^2}{2\delta^2}} e^{-m^2 y^2/(2\delta^2)} {}_1F_1\left(-\frac{m^2}{4} + \frac{1}{4}, \frac{1}{2}, m^2 \frac{y^2}{\delta^2}\right), \quad (\text{A.11})$$

where coefficients C_m are taken from Eq. (A.10). For the case C^* , the first ten coefficients are: 1.2008, -0.2991, 0.1608, -0.1074, 0.0796, -0.0627, 0.0515, -0.0435, 0.0375, -0.0329.

Appendix B. Free surface boundary conditions

There are a few implementations of free boundary conditions [49,50]. However, we developed the easy solver to impose the free surface boundary conditions at the complicated surface of the bubble. The reason is to impose the symmetric boundary conditions.

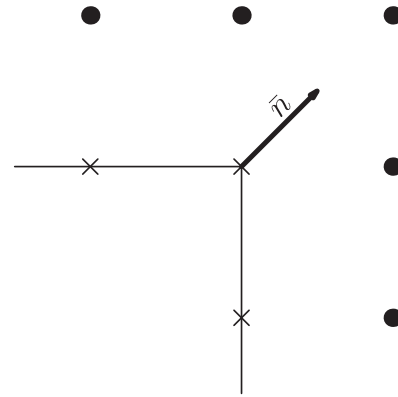


Fig. B.17. Free-surface boundary condition represented in the lattice Boltzmann method. Boundary nodes are depicted by crosses, and fluid nodes are represented by dots. The populations at the corner boundary nodes are essentially the populations of the fluid node, but in a different order.

Because the boundary is a staircase approximation, one can find the normal to the boundary which is always located by the angle of multiple of 45 degrees, see Fig. B.17. The finding identification of normals can be done automatically by a simple code. Imposing the symmetric boundary conditions requires $U_{n,F} = -U_{n,B}$ and $U_{\tau,F} = U_{\tau,B}$. We can copy populations in a certain order to do it, for example $f_{B,i} = f_{F,i}$, where c_i and c_i are complementary directions, where $c_{i,n} = -c_{i,n}$ and $c_{i,\tau} = c_{i,\tau}$, where $c_{i,n} = (\mathbf{c}_i \cdot \mathbf{n})\mathbf{n}$ and $c_{i,\tau} = \mathbf{c}_i - (\mathbf{c}_i \cdot \mathbf{n})\mathbf{n}$. One can check by taking the definition of velocity $\rho \mathbf{u} = \sum_i f_i \mathbf{c}_i$ and substituting it in the relationships above, that the normal velocities are canceled, i.e. $U_{n,F} = -U_{n,B}$, but the tangential velocity component is conserved, $U_{\tau,F} = U_{\tau,B}$.

References

- [1] M.D. Giavedoni, F.A. Saita, The axisymmetric and plane cases of a gas phase steadily displacing a Newtonian liquid – a simultaneous solution of the governing equations, *Phys. Fluids* 9 (8) (1997) 2420–2428.
- [2] J.M. van Baten, R. Krishna, CFD simulations of mass transfer from Taylor bubbles rising in circular capillaries, *Chem. Eng. Sci.* 59 (2004) 2535–2545.
- [3] M.T. Kreutzer, F. Kapteijn, J.A. Moulijn, J.J. Heiszwolf, Multiphase monolith reactors: chemical reaction engineering of segmented flow in microchannels, *Chem. Eng. Sci.* 60 (2005) 5895–5916.
- [4] G. Bercic, A. Pintar, The role of gas bubbles and liquid slug lengths on mass transport in the Taylor flow through capillaries, *Chem. Eng. Sci.* 52 (21–22) (1997) 3709–3719.
- [5] F.P. Bretherton, The motion of long bubbles in tubes, *J. Fluid Mech.* 10 (2) (1960) 166–188.
- [6] G.I. Taylor, Deposition of a viscous fluid on the wall of a tube, *J. Fluid Mech.* 10 (1961) 161–165.
- [7] J. Yue, L. Luo, Y. Gonthier, G. Chen, Q. Yuan, An experimental study of air–water Taylor flow and mass transfer inside square microchannels, *Chem. Eng. Sci.* 64 (2009) 3697–3708.
- [8] R. Gupta, D.F. Fletcher, B.S. Haynes, Taylor flow in microchannels: a review of experimental and computational work, *J. Comput. Multiphase Flows* 2 (2010) 1–32.
- [9] M.T. Kreutzer, M.G. van der Eijnded, F. Kapteijn, J.A. Moulijn, J.J. Heiszwolf, The pressure drop experiment to determine slug lengths in multiphase monoliths, *Catal. Today* 105 (2005) 667–672.
- [10] W.B. Kolb, R.L. Cerro, Film Flow in the space between a circular bubble and a square tube, *J. Coll. Int. Sci.* 159 (1993) 302–311.
- [11] T.C. Thulasidas, M.A. Abraham, R.L. Cerro, Bubble-train flow in capillaries of circular and square cross-section, *Chem. Eng. Sci.* 50 (2) (1995) 183–199.
- [12] D. Liu, S. Wang, Hydrodynamics of Taylor flow in noncircular capillaries, *Chem. Eng. Process.* 47 (2008) 2098–2106.
- [13] A. Kuzmin, M. Januszewski, D. Eskin, F. Mostowfi, J. Derksen, Three-dimensional binary-liquid lattice Boltzmann simulation of microchannels with rectangular cross-sections, *Chem. Eng. J.* 178 (2011) 306–316.
- [14] A.L. Hazel, M. Heil, The steady propagation of a semi-infinite bubble into a tube of elliptical or rectangular cross-section, *J. Fluid Mech.* 470 (2002) 91–114.
- [15] O. Keskin, M. Wornor, M. Soghan, T. Bauer, O. Deutchmann, R. Lange, Viscous co-current downward Taylor flow in a square mini-channel, *AIChE J.* 56 (7) (2010) 1693–1702.
- [16] S. Irandoust, S. Ertle, B. Andersson, Gas–liquid mass transfer in Taylor flow through a capillary, *Can. J. Chem. Eng.* 70 (1992) 115–119.

- [17] R. Higbie, The rate of absorption of a pure gas into a still liquid during short periods of exposure, *Trans. Am. Inst. Chem. Eng.* 31 (1935) 365–389.
- [18] A. Kuzmin, M. Januszewski, D. Eskin, F. Mostowfi, J. Derksen, Simulations of gravity-driven flow of binary liquids in microchannels, *Chem. Eng. J.* 171 (2) (2011) 646–654.
- [19] A. Onea, M. Worner, D. Cacuci, A qualitative computational study of mass transfer in upward bubble train flow through square and rectangular mini-channels, *Chem. Eng. Sci.* 64 (7) (2009) 1416–1435.
- [20] U. Frisch, D. d'Humières, B. Hasslacher, P. Lallemand, Y. Pomeau, J.-P. Rivet, Lattice gas hydrodynamics in two and three dimensions, *Complex Syst.* 1 (1987) 649–707.
- [21] G.R. McNamara, G. Zanetti, Use of the Boltzmann equation to simulate lattice-gas automata, *Phys. Rev. Lett.* 61 (20) (1988) 2332–2335.
- [22] F.J. Higuera, J. Jimenez, Boltzmann approach to lattice gas simulations, *Europhys. Lett.* 9 (7) (1989) 663–668.
- [23] F.J. Higuera, S. Succi, R. Benzi, Lattice gas dynamics with enhanced collisions, *Europhys. Lett.* 9 (4) (1989) 345–349.
- [24] D. Yu, R. Mei, L.-S. Luo, W. Shyy, Viscous flow computations with the method of lattice Boltzmann equation, *Prog. Aerospace Sci.* 39 (2003) 329–367.
- [25] X. Shan, H. Chen, Simulation of nonideal gases and gas–liquid phase transitions by the lattice Boltzmann equation, *Phys. Rev. E* 49 (4) (1994) 2941–2948.
- [26] M.R. Swift, W.R. Osborn, J.M. Yeomans, Lattice Boltzmann simulation of nonideal fluids, *Phys. Rev. Lett.* 75 (5) (1995) 831–834.
- [27] A.K. Gunstensen, D.H. Rothman, S. Zaleski, G. Zanetti, Lattice Boltzmann model of immiscible fluids, *Phys. Rev. A* 43 (8) (1991) 4320–4327.
- [28] P. Yuan, L. Schaefer, A thermal lattice Boltzmann two-phase flow model and its application to heat transfer problems – Part 2: Integration and validation, *J. Fluids Eng.* 128 (2006) 151–156.
- [29] R. Zhang, H. Chen, Lattice Boltzmann method for simulations of liquid–vapor thermal flows, *Phys. Rev. E* 67 (066711) (2003) 1–6.
- [30] P.J. Dellar, Lattice kinetic formulation for ferrofluids, *J. Stat. Phys.* 121 (2005) 105–118.
- [31] G. Falcucci, G. Chiatti, S. Succi, A.A. Mohamad, A. Kuzmin, Rupture of a ferrofluid droplet in external magnetic fields using a single-component lattice Boltzmann model for nonideal fluids, *Phys. Rev. E* 79 (056706) (2009) 1–5.
- [32] I. Ginzburg, Equilibrium-type and link-type lattice Boltzmann models for generic advection and anisotropic-dispersion equation, *Adv. Wat. Res.* 28 (2005) 1171–1195.
- [33] I. Ginzburg, Generic boundary conditions for lattice Boltzmann models and their application to advection and anisotropic dispersion equations, *Adv. Wat. Res.* 28 (2005) 1196–1216.
- [34] I. Ginzburg, Variably saturated flow described with the anisotropic lattice Boltzmann methods, *Comput. Fluids* 35 (2006) 831–848.
- [35] M. Yoshino, T. Inamuro, Lattice Boltzmann simulations for flow and heat/mass transfer problems in a three-dimensional porous structure, *Int. J. Num. Meth. Fluids* 43 (2003) 183–198.
- [36] J.J. Derksen, Simulations of lateral mixing in cross-channel flow, *Comput. Fluids* 39 (2010) 1058–1069.
- [37] P.L. Bhatnagar, E.P. Gross, M. Krook, A model for collision processes in gases. I: Small amplitude processes in charged and neutral one-component systems, *Phys. Rev.* 94 (3) (1954) 511–525.
- [38] I. Ginzburg, F. Verhaeghe, D. d'Humières, Two-relaxation-time lattice Boltzmann scheme: about parametrization, velocity, pressure and mixed boundary conditions, *Commun. Comput. Phys.* 3 (2) (2008) 427–478.
- [39] I. Ginzburg, D. d'Humières, Multireflection boundary conditions for lattice Boltzmann models, *Phys. Rev. E* 68 (066614) (2003) 1–30.
- [40] I. Ginzburg, Lattice Boltzmann modeling with discontinuous collision components: hydrodynamic and advection-diffusion equations, *J. Stat. Phys.* 126 (1) (2007) 157–206.
- [41] D. d'Humières, I. Ginzburg, Viscosity independent numerical errors for lattice Boltzmann models: from recurrence equations to “magic collision numbers”, *Comput. Math. Appl.* 58 (5) (2009) 823–840.
- [42] B. Servan-Camas, F.T.-C. Tsai, Lattice Boltzmann method with two relaxation times for advection-diffusion equation: third order analysis and stability analysis, *Adv. Wat. Res.* 31 (2008) 1113–1126.
- [43] I. Ginzburg, Consistent lattice Boltzmann schemes for the Brinkman model of porous flow and infinite Chapman–Enskog expansion, *Phys. Rev. E* 77 (066704) (2008) 1–12.
- [44] I. Ginzburg, D. D'Humières, A. Kuzmin, Optimal stability of advection-diffusion lattice Boltzmann models with two relaxation times for positive/negative equilibrium, *J. Stat. Phys.* 139 (6) (2009) 1090–1143.
- [45] A. Kuzmin, I. Ginzburg, A.A. Mohamad, The role of the kinetic parameter in the stability of two-relaxation-time advection-diffusion lattice Boltzmann schemes, *Comput. Math. Appl.* 61 (2011) 3417–3442.
- [46] S. Chapman, T.G. Cowling, *The Mathematical Theory of Non-uniform Gases*, third ed., Cambridge University Press, Cambridge, 1995.
- [47] A.D. Polyinin, A.M. Kutepov, A.V. Vyazmin, D.A. Kazenin, *Hydrodynamics, Mass and Heat Transfer in Chemical Engineering*, Taylor and Francis, 2002.
- [48] M. Abramowitz, I. Stegun (Eds.), *Handbook of Mathematical Functions with Formulas* Graphs and Mathematical Tables*, National Bureau of Standards, 1964.
- [49] I. Ginzburg, K. Steiner, A free-surface lattice Boltzmann method for modelling the filling of expanding cavities by Bingham fluids, *Phil. Trans. R. Soc. Lond. A* 360 (2002) 453–466.
- [50] X. Yin, D.L. Koch, R. Verberg, Lattice-Boltzmann method for simulating spherical bubbles with no tangential stress boundary conditions, *Phys. Rev. E* 73 (2006) 1–13.